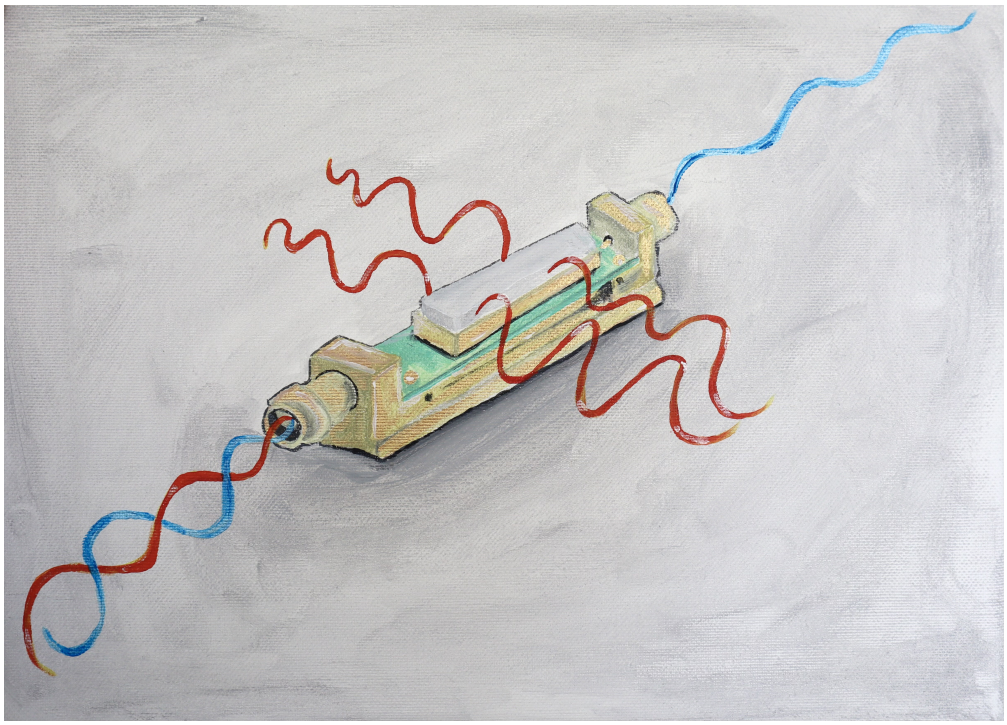

Miniaturized High-Energy Radiation Drain Filters for Quantum Computing Applications

Design, Characterization and Analysis of Miniaturized HERD Filters

Master's thesis in Wireless, Photonics and Space Engineering

LINUS ANDERSSON

DEPARTMENT OF MICROTECHNOLOGY AND NANOSIENCE

CHALMERS UNIVERSITY OF TECHNOLOGY
Gothenburg, Sweden 2023
www.chalmers.se

Master's thesis 2023

Miniaturized High-Energy Radiation Drain Filters for Quantum Computing Applications

Design, Characterization and Analysis of Miniaturized HERD Filters

LINUS ANDERSSON

CHALMERS
UNIVERSITY OF TECHNOLOGY

Department of Microtechnology and Nanosience
Division of Quantum Technology
202Q-LAB
Chalmers University of Technology
Gothenburg, Sweden 2023

Miniaturized High-Energy Radiation Drain Filters for Quantum Computing Applications
Design, Characterization and Analysis of Miniaturized HERD Filters
LINUS ANDERSSON

Supervisor: Robert Rehammar, Microtechnology and Nanoscience
Examiner: Simone Gasparinetti, Microtechnology and Nanoscience

Master's Thesis 2023
Department of Microtechnology and Nanoscience
Division of Quantum Technology
202Q-LAB
Chalmers University of Technology
SE-412 96 Gothenburg
Telephone +46 31 772 1000

Cover: Illustration of the inner parts of the device designed in this thesis, where the hot (red) high-frequency radiation is extracted by the filter and the cold (blue) low frequency signal remains intact.

Typeset in LaTeX
Printed by Chalmers Reproservice
Gothenburg, Sweden 2023

Miniaturized High-Energy Radiation Drain Filters for Quantum Computing Applications
Design, Characterization and Analysis of Miniaturized HERD Filters
LINUS ANDERSSON
Department of Microtechnology and Nanosience
Chalmers University of Technology

Abstract

Quantum Processing Units (QPUs) using superconducting qubits are known for their sensitivity to various types of radiation and many different aspects are being worked on in order to increase their resilience against noise. Superconducting qubits are especially sensitive frequencies with energy exceeding twice the superconducting energy gap of the superconductor. Above this frequency, Copper-pairs start to break, which partially disrupts superconductivity and degrades the performance of the QPU. In order to tackle this problem, a new type of low pass filtering technique called High Energy Radiation Drain (HERD) has been developed at at Chalmers University of Technology. Unlike previously employed filters relying on absorptive materials and resonant circuits to block high-frequency photons, this novel filtering technique overcomes the trade-off between low losses in the passband and high attenuation in the stopband. However, the filter is relatively large compared other filtering techniques, which makes it less suitable for high qubit density systems. In this thesis, we focus on the miniaturization of the HERD filtering technology and present two devices which have a reduced size of 32-57% and 47% respectively compared to their predecessor. The first device, implemented in printed circuit board technology, is manufactured and characterized with a resulting insertion loss of more than 40 dB above 80 GHz and an insertion loss of less than 0.29 dB below 8 GHz, measured at 77 K. The results show good agreement between measurements and simulations. In addition, a software is developed for performing eigenmode field decomposition of the filtering structure, which is used to better understand how the field couples to the filtering structure inside the prototype. The insights obtained from simulations and the field decomposition is then used to design the second device, a miniaturized coaxial HERD filter. The results shows that the HERD filtering technique can be made suitable for high qubit density systems where further miniaturization beyond this thesis should be possible.

Keywords: quantum computing, quasiparticles, filter design, infrared radiation, HERD filter, simulation and modelling, mode decomposition, filter optimization.

Acknowledgements

First off, I would like to thank my supervisor Robert Rehammar and my examiner Simone Gasparinetti for allowing me to pursue this project for the past few months. To Robert, thank you for being a great teacher and for being explorative and open minded when approaching different problems. To Simone, thanks for allowing me to be a part of your group both during this thesis, but also during my time as an amanuensis. I am very grateful for the experience this has given me.
I would also like to thank the entire 202Q-lab group. It has been a pleasure to work in such a skilled and motivated team. Special thanks to Ingrid Strandberg for her valuable input in the development of the eigenmode decomposition method. I would also like to thank Lars Jönsson for fruitful discussions and a great job of machining all the parts to the prototype.
Last but not least I would like to thank my mom and sister for their never ending support, and Alice, for standing by my side at all times.

Linus Andersson, Gothenburg, June 2023

Acronyms

AlN Aluminium Nitride.

CPW Coplanar Waveguide.

DUT Device Under Test.

EM Electromagnetic.
ENIG Electroless Nickel Immersion Gold.

HERD High Energy Radiation Drain.
HW Hollow Waveguide.

IBC Impedance Boundary Condition.

LN2 Liquid Nitrogen.
LTCC Low Temperature Co-Fired Ceramic.

NPTH Non Plated Through Hole.

PCB Printed Circuit Board.
PEC Perfect Electric Conductor.

QP Quasiparticle.

SBC Scattering Boundary Condition.
SLSQP Sequential Least Squares Programming.
SNR Signal to Noise Ratio.

TE Transverse Electric.
TEM Transverse Electromagnetic.
TM Transverse Magnetic.

VNA Vector Network Analyzer.

Contents

List of Figures

List of Tables

1

Introduction

The field of quantum computation is advancing rapidly, with significant scientific and industrial efforts devoted to constructing the first truly useful machines. In this pursuit, a diverse range of scientific disciplines have united to advance development all the way from classical computer science to the physics of individual particles. There are several distinct platforms for constructing a quantum computer, with superconducting qubits as one of the most promising candidates [1]. These qubits rely on superconductivity and a particular circuit component called a Josephson junction [2]. By incorporating this nonlinear element with other circuit elements, it is possible to design oscillator circuits that behave like atoms, where each energy level of the oscillator can be addressed distinctly by the excitation of a microwave signal [3]. This circuit can then be utilized as a qubit by treating it as a two-level system.

Due to the quantum mechanical properties of superposition and entanglement, many qubits can be electromagnetically coupled to each other to form an increasingly larger set of quantum states of the circuit. This property gives the quantum computer an advantage compared to classical computers. For a classical computer with N number of bits, the number of possible arrangements of zeroes and ones are 2^N. However, on a classical computer, a logic gate can only do operations on one of these combinations at the time. For a quantum computer, one can, in principle, have a superposition of all 2^N quantum states at the same time, which can simultaneously be operated upon [3]. This could potentially result in a huge parallelization capability, representing the fundamental strength of quantum computers. Nevertheless, building a quantum computer is an intricate process. The same principles that enable the interaction with the qubits also pose a formidable challenge for their construction.

Except for the microwave signals that manipulate the qubits, other sources of radiation can interact with and affect the qubits through numerous different physical mechanisms [4]. This limits the amount of computations that can be performed. The quality of the qubits and their environment is often characterised by measuring the time for which the qubit can stay coherent. These are the longitudinal relaxation time T_1 and the transverse relaxation time T_2. Different types of noise affect these two figures of merit differently and to improve them one needs to work on various aspects such as electromagnetic shielding, qubit design and better control methods [4].

One source of such noise is the generation of Quasiparticle (QP) inside of the super-

conductor [5]. The generation of a QPs occurs when a Cooper pair is broken due to interaction with a photon of high enough energy, higher than twice the superconducting gap of the thin film used on the chip. For aluminum, which is a commonly used material for thin films, the superconducting gap is around 80 GHz. It has been shown that QP generation can have a significant impact on qubit energy dissipation [6]. In a recent study from IBM [7], different shielding setups are tested on different qubit designs which shows that high frequency radiation from the environment does indeed affect the performance of the system as a hole.

Despite having excellent shielding from external radiation, high frequency photons can still enter the sample through the interconnections to the room temperature electronics. A common way to prevent such radiation from reaching the qubits has been to use absorptive filters that have high absorption in the Cooper pair breaking frequency range. These are typically made with materials such as Eccosorb® or copper-powder infused epoxy [8]. However, such filters have a major drawback in that they present high losses in the passband. In general, this is not a problem on the input lines to the qubits since attenuation of the control signals are anyway necessary [9]. However, high losses in the passband makes it practically impossible to use these filters on the output lines, where low losses are of utmost importance.

A candidate for bridging the gap between low loss in the passband and high attenuation in the stopband is a new filtering technique called High Energy Radiation Drain (HERD) [10]. The HERD filter relies on the excitation of Hollow Waveguides (HWs) which are coupled to a regular coaxial structure. Below the cutoff frequency of the HWs the electromagnetic fields are unaffected which results in a very low loss and low ripple passband. As the frequency reaches above cutoff frequency of the HWs, the field starts to leak through the HWs and results in a low pass filter with a wide stopband with high attenuation. However, the prototype presented in [10] is significantly larger compared to typical absorptive type filters [11] [12]. This makes the HERD filter less suitable to use in systems with a high number of qubits where line density is high.

The objective of this thesis is to develop and evaluate a miniaturized HERD filter suitable for use in quantum computing applications. This will include looking at different technologies and materials which could serve as a candidate for such a filter. When a technology has been chosen, the methods of implementing a HERD filter will be investigated. Additionally, the study will address the limitations associated with the HERD filtering technology and try to better understand how to improve the coupling to the HWs in the stopband. This will be done by studying the mode composition inside the HWs to see what modes are more prominent than others. Performing such an analysis may bring more understanding on how the field in the stopband couples to the electrically large apertures.

The finished design should be integrated into a package that can be mounted inside of a cryostat. The microwave characterisation of the filter will be done by measuring the scattering parameters with a Vector Network Analyzer (VNA). These measurements will be performed in room temperature, but also in a cold environment such as liquid nitrogen at 77 K. The reason for doing measurements in a cold environment is to study how the thermal shrinking affects the performance of the filter and to make

sure that the design can withstand the mechanical stress caused by the shrinking.

2

Theory

In this section, the theory underlining the working principles of the HERD filtering technology is described. First, a short overview of the electromagnetic boundary conditions is presented. Understanding these conditions are central to the concept of eigenmode propagation in rectangular waveguides. The different sources of electromagnetic loss mechanisms are described, followed by the solutions to Maxwell's equations for a given rectangular waveguide in conjunction with a discussion about the orthogonal properties of these solutions. Next, the working principles of HERD filters are described. The last section of this chapter is devoted to describing the method of field decomposition and how it can bring further understanding to how different eigenmodes couple to the HERD filtering structure.

2.1 Electromagnetic Boundary Conditions

To understand how electromagnetic waves behave in different materials for a specific geometry, it is important to understand the electromagnetic boundary conditions. When solving Maxwell's equations, the problem is usually divided into the different regions containing different materials and geometry. When the solutions in these regions are obtained, the boundary conditions are used stitch the solutions together for the entire space. Hence, the electromagnetic boundary conditions are essential, not only to obtain the fields, but also to gain insight about why certain devices behave as they do. By first considering a boundary between two dielectric materials, we know that the magnetic surface current $\vec{M}_s$, electric surface current $\vec{J}_s$ and the surface charge ρ_s is zero [13]. In this case, the fields in the different media relate to each other according to the following equations

$$\hat{n} \times \vec{E_1} = \hat{n} \times \vec{E_2} \tag{2.1}$$

$$\hat{n} \cdot \vec{D_1} = \hat{n} \cdot \vec{D_2} \tag{2.2}$$

$$\hat{n} \times \vec{H_1} = \hat{n} \times \vec{H_2} \tag{2.3}$$

$$\hat{n} \cdot \vec{B_1} = \hat{n} \cdot \vec{B_2} \tag{2.4}$$

where the subscripts on the fields indicate on which side of the boundary they are defined. In 2.1, it can be seen that the tangential electric field components across the boundary is continues. A similar relation between the magnetic field can be

seen in (2.3). The second equation (2.2) shows that the normal components of the electric displacement fields are continues between the two media. The same applies for the magnetic flux density in (2.4).

The second boundary of interest is the boundary between a dielectric and a Perfect Electric Conductor (PEC). This boundary condition is of high importance when dealing with waveguides made of metal, since this is often a useful approximation of a metal. The field relations in this case become

$$\hat{n} \times \vec{E} = 0 \tag{2.5}$$

$$\hat{n} \cdot \vec{D} = \rho_s \tag{2.6}$$

$$\hat{n} \times \vec{H} = \vec{J}_s \tag{2.7}$$

$$\hat{n} \cdot \vec{B}_1 = 0 \tag{2.8}$$

where the tangential electric field components are zero at the boundary. For the normal component of electric displacement field, it can be seen that the amount of dicontinuity is proportional to the surface charge density at the boundary. The tangential magnetic field is equal to the current density at the PEC boundary and the normal components of the magnetic flux density is zero.

2.2 Dielectric and Conductive Losses

In most waveguides, losses are dominated by conductive and dielectric losses. The electric displacement field inside a dielectric can be written as

$$\vec{D} = \epsilon \vec{E} + \vec{P}_e \tag{2.9}$$

where $\vec{P}_e = \epsilon \chi_e \vec{E}$ is called the polarization vector. The parameter χ_e is the electric susceptibility and is said to be linear if independent of the electric field $\vec{E}$. This quantity can be complex valued if the material is lossy and is typically incorporated in the complex permittivity of the material

$$\epsilon = \epsilon' - j\epsilon'' = \epsilon_0(1 + \chi_e) \tag{2.10}$$

where imaginary part ϵ'' accounts for power losses in the dielectric. The losses can then be further divided into dielectric and metallic losses due to displacement currents and lossy currents, seen in the permittivity as

$$\epsilon = \epsilon' - j\epsilon'' - j\sigma/\omega = \epsilon_0\epsilon_r(1 - j\tan\delta) \tag{2.11}$$

where σ is the conductivity and the term $\tan\delta$ is the loss tangent of the material. The loss tangent is often specified in the electrical properties of a material and incorporates both displacement current loss and metallic losses.

Similarly, a material can also represent magnetic losses through the complex permeability defined as

$$\mu = \mu_0(1 - \chi_m) = \mu' - j\mu'' \tag{2.12}$$

where χ_m is the magnetic susceptibility whose imaginary part is related to the magnetic losses in the material.

For an electromagnetic wave traveling in or close to a material with high conductivity, the electric current will be concentrated towards the surface. This effect is called the skin effect and is characterized by a the skin depth, which for a good conductor is given by

$$\delta_s = \sqrt{\frac{2}{\omega\mu\sigma}} \tag{2.13}$$

which is a measure of the depth for which the electric field has penetrated into the metal and decayed with a factor of e^{-1}. Hence, most of the conductive losses coming from the metal will be due to the conductivity close to the metal surface. Interestingly, by allowing the conductivity to approach infinity, it can be seen that the skin effect tends to zero. It should also be noted that the skin depth decreases with an increase of frequency.

In microwave applications it is common to describe the power loss in a metal in terms of a surface resistance. The surface resistance of a conductor is defined as

$$R_s = \frac{1}{\sigma\delta_s} \tag{2.14}$$

which comes from the good conductor approximation [13]. Another important factor of consideration, typically more so at millimeter wave frequencies, is the surface roughness of a conductor. Models exist for how the surface resistance depends on the root mean square Δ_{rms} of the surface roughness [14], where the geometry of the roughness is modelled in a sawtooth pattern. There is also another model, the snowball modell, for which the roughness geometry is modelled as spherical bumps in the metal [15]. Both models can be used to estimate the increase of surface resistance due to the surface roughness of a conductor.

Since HERD filters are used in cryogenic applications, it is interesting to know how the conductivity of normal metals, such as copper, changes when cooled down to cryogenic temperatures. Measurements performed by Rehammar et al. at the division of Quantum Technolgy at Chalmers University of Technology have observed conductivity of $\sigma_{77K} \approx 1.89 \cdot 10^9$ S/m at 77 K of Tin plated copper on RO4350B substrate. This is about two orders of magnitude higher than bulk copper in room temperature at $\sigma_{RT} = 5.813 \cdot 10^7$ S/m stated in [13].

2.3 Rectangular Waveguides

In a rectangular waveguide, the solutions to the wave equation are a discrete set of eigenmodes. The derivation of these solutions is presented in many famous textbooks and will not be included in this section[13][16]. However, the central concept underlining the derivation is that due to the boundary condition in (2.5), only multiples of half wavelengths can be supported in the transverse directions of the field propagation. Each solution, or mode, has a certain cut off frequency above which it can propagate inside the waveguide. For a lossless case, the propagation constant is defined as

$$\gamma = j\beta \tag{2.15}$$

where β is the phase constant of the mode, defined as

$$\beta = \sqrt{k^2 - k_c^2} \tag{2.16}$$

where $k = \omega\sqrt{\epsilon\mu}$ is the wavenumber of the medium and k_c is the cutoff wavenumber. The cut off wavenumber depends only on the geometry of the waveguide. In a rectangular waveguide it is given by

$$k_c = \sqrt{\left(\frac{\pi m}{a}\right)^2 + \left(\frac{\pi n}{b}\right)^2} \tag{2.17}$$

where a is the width and b is the height of the waveguide where $\{m, n\} = 0, 1, 2, ...$ The cut off frequency of the waveguide can then be calculated as

$$f_c = \frac{k_c}{2\pi\sqrt{\epsilon\mu}} \tag{2.18}$$

It can be seen from (2.16) that an electromagnetic wave with a frequency below f_c will have an imaginary phase constant. Consequently, a wave propagating along the z-axis with the factor $e^{\gamma z}$ and a frequency lower than f_c will vanish inside the waveguide.

It is common to define the coordinate system of the rectangular waveguide so that the width of the waveguide coincides with the x-axis and the height lies along the y-axis. The eigenmodes can be divided into to types of modes; Transverse Electric (TE) and Transverse Magnetic (TM). What characterizes these modes is that they either have or do not have an electric or magnetic field component in the direction of propagation. The TE modes are characterized by its non-zero z-component of the magnetic field and takes the following form

$$\vec{E}(x, y) = \begin{bmatrix} E_x(x, y), & E_y(x, y), & 0 \end{bmatrix} \tag{2.19}$$

$$\vec{H}(x, y) = \begin{bmatrix} H_x(x, y), & H_y(x, y), & H_z(x, y) \end{bmatrix} \tag{2.20}$$

where the electric field components are found to be

$$E_x = \frac{j\omega\mu n\pi}{k_c^2 a} \cos\frac{m\pi x}{a} \sin\frac{n\pi y}{b} \tag{2.21}$$

$$E_y = \frac{-j\omega\mu m\pi}{k_c^2 a} \sin\frac{m\pi x}{a} \cos\frac{n\pi y}{b} \tag{2.22}$$

with the magnetic field components found as

$$H_x = \frac{j\beta m\pi}{k_c^2 a} \sin\frac{m\pi x}{a} \cos\frac{n\pi y}{b} \tag{2.23}$$

$$H_y = \frac{j\beta m\pi}{k_c^2 a} \sin\frac{m\pi x}{a} \cos\frac{n\pi y}{b} \tag{2.24}$$

$$H_z = \cos\frac{m\pi x}{a} \cos\frac{n\pi y}{b} \tag{2.25}$$

The TM modes are characterized by the non-zero z-component of the electric field from where the field take the form of

$$\vec{E}(x,y) = \Big[E_x(x,y), \quad E_y(x,y), \quad E_z(x,y)\Big] \tag{2.26}$$

$$\vec{H}(x,y) = \Big[H_x(x,y), \quad H_y(x,y), \quad 0\Big] \tag{2.27}$$

with the electric field components defined as

$$E_x = \frac{-j\beta m\pi}{k_c^2 a} \cos\frac{m\pi x}{a} \sin\frac{n\pi y}{b} \tag{2.28}$$

$$E_y = \frac{-j\beta n\pi}{k_c^2 b} \sin\frac{m\pi x}{a} \cos\frac{n\pi y}{b} \tag{2.29}$$

$$E_z = \sin\frac{m\pi x}{a} \sin\frac{n\pi y}{b} \tag{2.30}$$

and the magnetic field components as

$$H_x = \frac{j\omega\epsilon n\pi}{k_c^2 b} \sin\frac{m\pi x}{a} \cos\frac{n\pi y}{b} \tag{2.31}$$

$$H_y = \frac{-j\omega\epsilon m\pi}{k_c^2 a} \sin\frac{m\pi x}{a} \cos\frac{n\pi y}{b} \tag{2.32}$$

A useful property of each TE_{mn} and TM_{mn} mode is that they are orthogonal [16]. The longitudinal field components are orthogonal if they satisfy

$$\iint_S E_{z,i} E_{z,j} dS = 0 \tag{2.33}$$

were the subscripts i,j indicates two different eigenmodes and S is the cross sectional surface of the waveguide. For the transverse components, two modes $\vec{E}_i$ and $\vec{E}_j$, either TE or TM or a combination of both, are orthogonal because they fulfill

$$\iint_S \vec{E}_i \times \vec{H}_j^* dS = 0 \tag{2.34}$$

which shows that two different modes in the same waveguide carry their own power. It should be noted that the orthogonal properties only holds for perfectly conducting walls in the waveguide, but may still be an accurate approximation for practice where the conductive losses are small [17]. Since the fields are orthogonal and thus do not interact, the total field can be decomposed into a superposition of the eigenmodes propagating inside of the structure. A proof of the above orthogonality relations will not be presented here, but are presented rigorously in [17]. The orthogonality property will be utilized when analyzing the mode content inside the HERD filtering structure.

The time average power of a TE mode propagating through the waveguide cross section can be obtained by integrating the complex Poynting vector $\vec{S} = \frac{1}{2}\mathrm{Re}\vec{E} \times \vec{H}^*$

$$\begin{aligned} P_{avg}^{TE} &= \frac{1}{2}\mathrm{Re}\int_0^a \int_0^b \vec{E} \times \vec{H}^* \cdot \hat{z} dx dy \\ &= \frac{1}{2}\mathrm{Re}\int_0^a \int_0^b (E_x H_y^* - E_y H_x^*) dx dy \\ &= \frac{1}{2}\mathrm{Re}\frac{1}{Z_{TE}^*}\int_0^a \int_0^b (|E_x|^2 + |E_y|^2) dx dy \end{aligned} \tag{2.35}$$

where $Z_{\mathrm{TE}} = k\eta/\beta$ is the wave impedance of the waveguide, relating the transverse electric and magnetic vector components and $\eta = \sqrt{\mu/\epsilon}$ is the dielectric wave impedance. In a similar fashion, the power for TM modes is found to be

$$P_{avg}^{TM} = \frac{1}{2}\mathrm{Re}\frac{1}{Z_{TM}^*}\int_0^a \int_0^b (|E_x|^2 + |E_y|^2) dx dy \tag{2.36}$$

where $Z_{TM} = \beta\eta/k$ is the wave impedance relating the transverse electromagnetic field components. It should be noted, however, that the wave impedance for a propagating mode is purely real and the complex conjugate can be omitted in this case. For a evanescent wave, the wave impedance is purely imaginary and the time average power is therefore zero.

2.4 High Energy Radiation Drain Filters

The concept of HERD filters was first demonstrated using a air filled coaxial waveguide coupled to an array of HW [10]. This filter presented an insertion loss of 0.15

dB up to 12 GHz and 60 dB of attenuation above 70 GHz. The HWs was filled with PTFE dielectric slabs $\epsilon_r = 2.2$ in order to improve the coupling to the coaxial line. The slabs reduces the electrical size of the waveguide, effectively lowering the cut off frequency of the HW array, seen in (2.18). At low frequencies in the 4-8 GHz range, which is the typical band of interest for superconducting qubits, the electric field can not propagate inside the HWs, preventing the field from escaping the coaxial line. Evanescent modes excited in the HWs might still escape at these frequencies if the depth of the HWs are not sufficient. For a mode below cut off, the propagation constant in (2.16) will be complex, resulting in a dampening factor of

$$F(d) = e^{-\alpha d} \tag{2.37}$$

where $\alpha = \sqrt{k_c^2 - k^2}$ and d is the depth of the HW. The loss induced by evanescent tunneling can be estimated by

$$T = (1 - |F|^2)^N \tag{2.38}$$

where T is the filter transmission and N is the number of HWs coupled to the coaxial line. This is a very simplistic model and does not take into account the interference inside the waveguide or how well the field couples to the HWs. However, it still shows the main idea that the HW depth in relation to tunneling loss is a tradeoff that the HERD filter is suffering from.

2.5 Eigenmode Field Decomposition

In order to gain a deeper understanding of the coupling between the electromagnetic field in the main line of propagation and the HWs, it is worthwhile to investigate the specific eigenmodes that are being excited within the HWs. Eigenmode decomposition has been widely used in the field of optics, where it has been used to process optical signals in order to retrieve the signal phase information for few- and multimode fibers [18], [19]. Many different methods have been used, stretching from fast psuedo-matrix operations to machine learning in order to obtain the modal content in realtime [20], [21]. The same techniques have also been used to obtain the modal content of multimode laser systems as a proposed tool for design improvement [22]. In the HERD filters, the array of HWs are expected to be highly overmoded in the stopband. A more comprehensive understanding of the mode content within these structures could potentially be used to design better HERD filters. The assumptions in the following section is that the material inside the HW is linear and isotropic and that the walls are PEC.

From Section 2.3 we know that, due to orthogonality, the total electric field inside the waveguide can be decomposed into a superposition of all propagating eigenmodes

$$\vec{E}(x, y) = \sum_{n=1}^{N} c_n \vec{E_n}(x, y) \tag{2.39}$$

weighted by a complex amplitude c_n. Before multiplication of the complex amplitudes, the fields of each eigenmode are normalized so that the total power in each eigenmode is equal to unity. This results in a convenient interpretation of the complex amplitudes as the fraction of power in the corresponding eigenmode $|c_n|^2 = P_n$. Hence, we define a normalization coefficient

$$\xi_n = \sqrt{\sum_{m=0}^{M} I_n(x_m, y_m)} \tag{2.40}$$

where M is the number of points $(x_m,\, y_m)$ on a 2D grid and $I_n(x, y)$ is the power flow through the HW cross section for the n:th mode, given by

$$I_n(x, y) = \hat{z} \cdot \langle \vec{S} \rangle = \frac{1}{2} \operatorname{Re}(E_{x,n} H^*_{y,n} - E_{y,n} H^*_{x,n}) \tag{2.41}$$

which is the scalar product between the cross section normal and the time average Poynting vector $\langle \vec{S} \rangle$.

Consider a field $\vec{E}^s(x, y)$, where the superscript s indicate a simulated field, composed by an unknown set of propagating eigenmodes according to (2.39). By normalizing both the electric and magnetic field by the normalization coefficient in (2.40), the total power of the field will be unity. This also enforces that the sum of the complex amplitudes modulus squared is unity

$$\sum_{n}^{N} |c_n|^2 = 1 \tag{2.42}$$

The decomposition of the fields is accomplished by minimizing the following expression with respect to the complex amplitudes as

$$\min_{c_n} \left\{ \sum_{m=1}^{M} \left| \frac{1}{\xi_{tot}} \vec{E}^s(x_m, y_m) - \sum_{n=1}^{N} \frac{1}{\xi_n} c_n \vec{E}_n(x_m, y_m) \right|^2 \right\} \tag{2.43}$$

where M is the number of points on a 2D surface and N is the number of propagating eigenmodes in the waveguide. Note that only one outer sum is used here, since the data is assumed to be obtained in a 1D array representing the field data in points (x_m, y_m). As a figure of merit of the decomposition algorithm, the correlation between the intensities can be calculated according to

$$C = \left| \frac{\int\int \Delta I_s \Delta I_r dx dy}{\sqrt{\int\int \Delta I_s^2 dx dy \int\int \Delta I_r^2 dx dy}} \right| \tag{2.44}$$

where $\Delta I_j = I_j(x, y) - \bar{I}_j$ for $j = s, r$ and $\bar{I}_j$ is the mean of I_j. The subscripts $j = s, r$ stands for the simulated (s) and reconstructed (r) intensity.

The decomposition algorithm used in this thesis was implemented in Python by using the SciPy minimization routine with the Sequential Least Squares Programming

(SLSQP) method. The cost function to be minimized is (2.43). In order to test the functionality of the algorithm, a set of propagating eigenmodes was generated and weighted with a set of normalized random complex coefficients. The generated test field was then passed to the minimization algorithm in order to reconstruct the the randomly generated complex coefficients.

In the minimization, the fields of the propagating eigenmodes generated by the field components described in Section 2.3. This was done for an aperture of $a = 2$ mm and $b = 1.4$ mm filled with a dielectric with relative permittivity of $\epsilon_r = 6.8$. The decomposition was done for a field at 100 GHz which has 13 propagating eigenmodes. The results can be seen in Figures 2.1. The algorithm manages to find the complex coefficients and reconstruct the fields with a correlation between the test field intensity I_t and the reconstructed field intensity I_r of $C = 1$. Important to note is that when applying the decomposition algorithm to the simulation data, the theoretical field is solved in the same points as in the simulation which can be obtained from the simulation files. All the code and simulation data are available in [23].

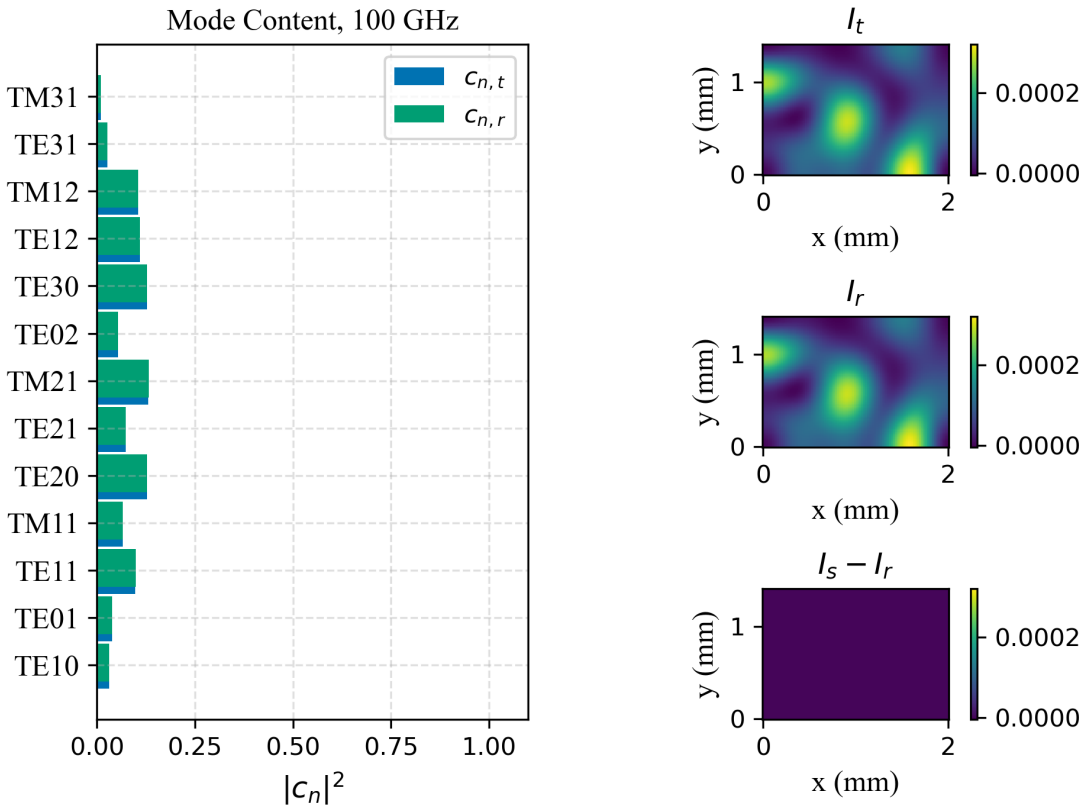

Figure 2.1: Reconstruction of random field at 100 GHz. The subscripts t,r is used to indicate the true and reconstructed complex amplitudes.

3

Methods

This chapter focuses on the development of a miniaturized HERD filter using Printed Circuit Board (PCB) technology. The use of PCB planar waveguides as the main guiding element are explored due to their thin substrates and metal layers, allowing for smaller waveguide design while maintaining a 50 Ω impedance. In addition, the chapter also discusses the selection of PCB technology over Low Temperature Co-Fired Ceramic (LTCC) circuits for cost-effectiveness. The PCB build-up for the HERD filter prototype is described, including the choice of materials and their properties. Electromagnetic simulation using commercial tools is employed to determine the dimensions of the waveguides, and the resulting S-parameters are presented. A first initial design concept of the HERD filtering structure, involving etched apertures and copper block waveguides, is explained, along with the selection of dielectric materials to improve performance. A design of a dedicated copper package to house the PCB and waveguide structure is presented, resulting in a significantly smaller size compared to the coaxial HERD filter presented in [10]. In addition, a miniaturized coaxial HERD filter is designed. This is followed by a section describing the measurement setup for measuring S-parameters used to characterize the filter performance. The chapter is concluded by the description of the field decomposition method used for studying the mode content inside the HERD HWs structures.

3.1 Design of a HERD Filter in PCB Technology

A promising start of implementing a miniaturized HERD filter is by using a planar circuit technology to realize the main guiding element. Planar circuit technologies, such as PCBs or LTCC, allows for very thin substrate and metal layers in the orders of tens to hundreds of micrometers. This makes it possible to design smaller waveguides while still maintaining a 50 Ω impedance. In addition, planar circuits are one of the most commonly used waveguide structures in the low GHz range and can be designed in many different configurations, such as microstrip, CPWs or striplines [13]. The manufacturing process is also highly accurate and cost-effective, with many different dielectric materials to choose from.

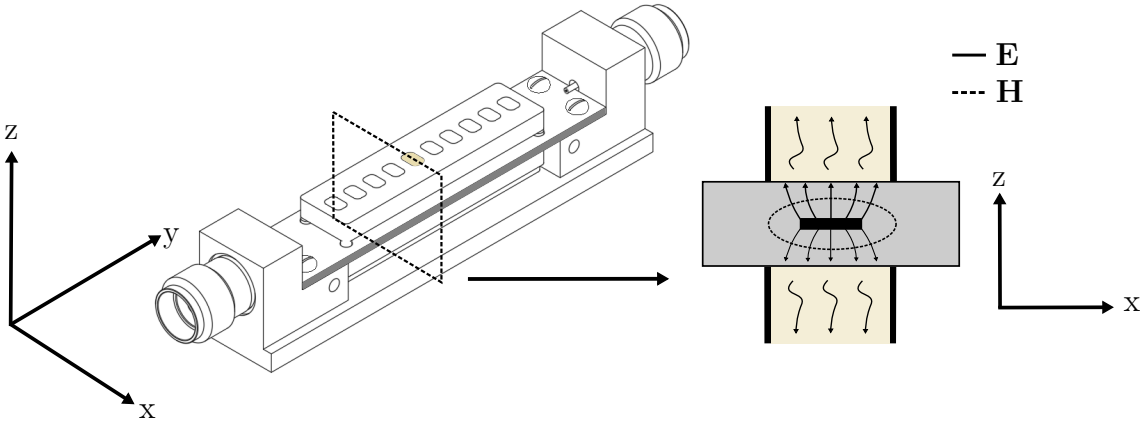

Figure 3.1: Filter design in relation to the coordinate system of choice and a cut in the xz-plane showing the stripline coupled to the HWs. The electric field lines for a stripline TEM mode can be seen in solid black with the magnetic field in dashed black.

By considering the field distribution of a coaxial waveguide, it can be seen that the electric field is perpendicular to the groundplane surrounding the center conductor. A planar waveguide showing a similar electric field distribution is the stripline. Using a stripline as the main guiding element will also allow the HWs to be placed on top and bottom of the stripline which, intuitively, should allow for a similar excitation of the HWs as in [10]. Generally, other planar waveguides, such as microstrip and CPW, do not have pure Transverse Electromagnetic (TEM) modes but rather quasi-TEM modes which have a small field component in the direction of propagation. As LTCC circuits turned out to be expensive for prototyping, although cost-effective for high volumes, the choice of technology for building a planar circuit HERD filter falls on PCB technology. PCBs are made by a combination of metal foils (typically copper) and dielectric substrates which are pressed together to form a multi layer structure. The number of layers in a PCB typically consist of an even number of copper layers with dielectric materials in between. In Figure 3.1, the image of the PCB HERD filter can be seen together with the definition of coordinate system in relation to the filter design.

When starting a PCB design, the first step is to determine the material build up. This is done by choosing a combination of two types of elements; cores and prepregs. Cores consists of a dielectric material sandwiched between two copper foils and are pre-laminated before production. Prepregs consists of a single sheet of dielectric which are pre-impregnated with a heat-activated resin that is used to join the dielectric with the metal on the laminates. Copper foil can be applied to the prepregs, but it is generally more expensive than laminating it with cores. This is also why most PCBs consists of an even number of metal layers. The details of the build up used in the work can be seen in Table 3.1.

To realize the PCB HERD filter, a build up using four layers consisting of two cores and a prepreg was chosen. The core material is the RO4350B from Rogers Corp. [24], which has a dielectric thickness of 254 μm and 35 μm thick copper. In

PCB Layer #	Material	Thickness [μm]	ϵ_r	tan(δ)
Metal 1	Cu (Core)	35	n/a	n/a
Substrate 1	Rogers RO4350B	254	3.48	0.0037
Metal 2	Cu (Core)	35	n/a	n/a
Substrate 2	Rogers RO4450F (prepreg)	100	3.52	0.004
Metal 3	Cu (Core)	35	n/a	n/a
Substrate 3	Rogers RO4350B	254	3.48	0.0037
Metal 4	Cu (Core)	35	n/a	n/a

Table 3.1: Material stack-up from top (Metal 1) to bottom (Metal 4) of PCB. When we talk about different layers of the PCB, we refer to the metal layers. The stripline is realized on metal layer 2.

between the cores, a 100 μm RO4450F prepreg from Rogers was chosen. Both of these materials are commonly used in microwave PCBs and are available with many manufacturers. The RO4350B core has a dielectric constant of $\epsilon_r = 3.48$ with a loss tangent of $\tan\delta = 0.0037$ at 10 GHz. The RO4450F prepreg has a dielectric constant of $\epsilon_r = 3.52$ with a loss tangent of $\tan\delta = 0.004$ at 10 GHz.

To obtain the 50Ω dimensions of the stripline, a model was built and simulated inside COMSOL Multiphysics [25]. The simulation was performed using numeric TEM ports and the conductors are modelled as PEC, which is generally the case throughout the entirety of the thesis if nothing else is mentioned. The conductors can also be modelled with IBCs where a finite conductivity as well surface roughness can be incorporated according to the models mentioned in Section 2.2. The dielectric material properties is taken from the built in models inside COMSOL for the above dielectric substrates. The resulting width of the stripline is 280 μm and the simulated S-parameters can be seen in Figure 3.2 along with the 3D model of the structure.

The HERD filtering structure will be accomplished by etching apertures in the top and bottom copper of the PCB. A milled copper structure containing the array of HWs will soldered on top of the aperture and will work as the filtering element. To allow the apertures to be smaller, a dielectric material can be used inside of the HWs. In [10], the cutoff frequency of the fundamental TE_{10} mode is around 20 GHz for an aperture of width $a = 4$ mm and a height $b = 5$ mm filled with a PTFE material with a dielectric constant of $\epsilon_r = 2.2$. A promising material with higher dielectric constant is Shapal Hi M Soft^{TM} [26], which is a machinable Aluminium Nitride (AlN) ceramic with a dielectric constant of $\epsilon_r = 6.8$. To maintain roughly the same cutoff frequency of the HWs, the initial dimensions of the apertures was set to $a = 2.8$ mm and $b = 2$ mm. In order for the insertion loss to not be dominated by evanescent waves tunneling through the HWs, the depth was set to $d = 4$ mm in order for (2.38) to stay above 0.99. As in [10], the HWs was terminated with SBC to make the simulation of the model more efficient.

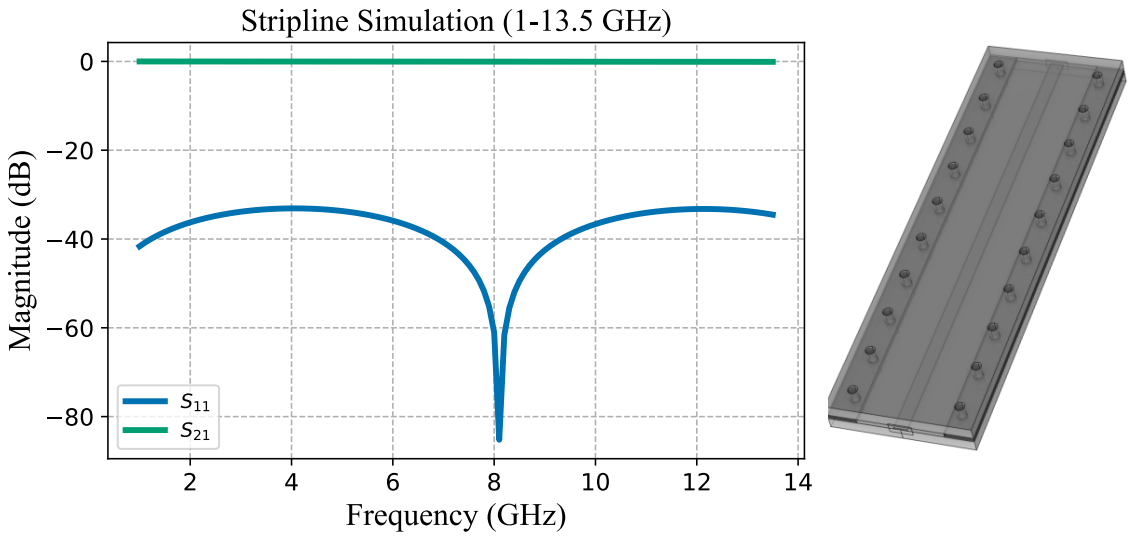

Figure 3.2: COMSOL simulation of a 10 mm stripline waveguide implemented in the proposed build up.

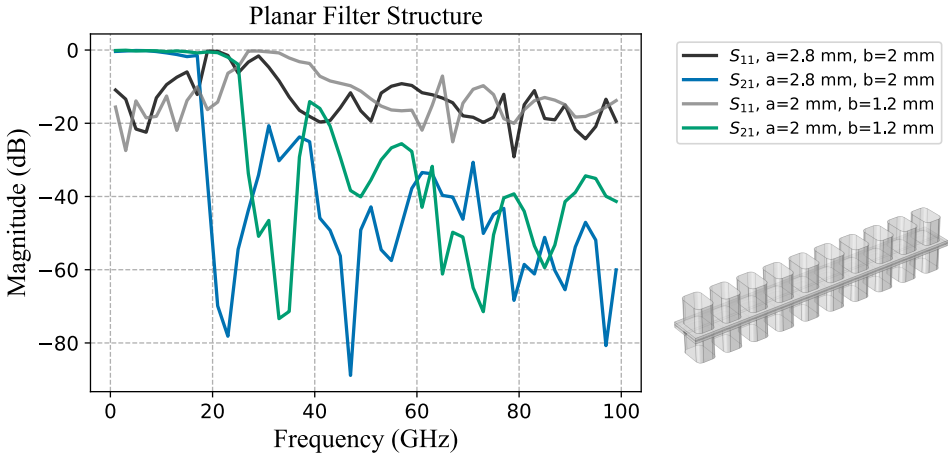

Figure 3.3: Parametric sweep of the aperture height of the HWs of the filter structure.

During simulations it was noticed that despite having the same cutoff frequency of the HWs as for the coaxial HERD filter, the planar HERD starts to leak for much lower frequencies. The filter presented in [10] starts to attenuate heavily at around 30 GHz, which suggests that the aperture size can be decreased for the planar HERD filter in order to achieve the same cutoff characteristics. Doing this should also improve the impedance mismatch caused by the added inductance resulting from the removal of metal for the apertures in the top and bottom ground planes. By decreasing the width $a = 2$ mm, the fundamental TE_{10} mode cutoff frequency becomes 28.7 GHz. Increasing the cutoff frequency also means that the depth of the

HWs can be decreased to $d = 2.6$ mm in order to keep the tunneling losses $|F(d)|^2$ below 0.001. The resulting dimension of the apertures was set to $a = 2$ mm and $b = 1.4$ mm.

As mentioned above, the HWs are terminated with SBC in the simulation model. To verify that this is viable method, the filter model HWs are also terminated by absorbing material in the simulation models. In this case, the absorbing material is modelled after the Laird MF-190 absorber [27], which has a permittivity with a real and imaginary part of $\epsilon' = 26.3$ and $\epsilon'' = 0.8$ respectively. The permeability has a real and imaginary part of $\mu' = 1.4$ and $\mu'' = 1$ respectively. The data is taken from the datasheet and is specified at 18 GHz. For the design, the Laird Eccosorb MS-24 absorbtive foam is used, which is a carbon based absorptive foam. Material data on this material is not detailed. Hence, the data presented for Laird MF-190 was used in the simulations instead.

After the design of the filtering structure, the rest of the device needs to be designed in order for the fields to enter the HERD region. For example, the stripline can not be excited directly by a connector and have to be connected to an external waveguide. Therefore, an intermediate CPW with a via transition to the stripline was designed. The resulting dimensions of the CPW 480 μm with a gap to the groundplane of 300 μm. The transition between the waveguides was carefully modelled and designed in order to maintain 50Ω impedance. During the simulations of a model with the SMA connector exciting the CPW, it was noticed that a mismatch occurs due to a capacitive behaviour near the excitation. In order to achieve good matching between the SMA connector pin and the CPW, a short section of the CPW was narrowed down to increase inductance locally, which balances out the capacitance added by the SMA pin. The PCB was designed in KiCad [28]. To ensure that the HW blocks solder well to the PCB, solder mask is added around the apertures. The PCB is plated with a Electroless Nickel Immersion Gold (ENIG) finish. This finish has significant loss at microwave frequencies [29], with room temperature conductivity stretching between $10^5 - 10^6$ S/m. Pure gold coating is more expensive and rarely available by cheaper manufacturers. Hence, ENIG was used for the prototype in this thesis. It is still a very common and lead free finish used by many PCB manufacturers. Production of the PCB was done by Eurocircuits and the finished PCB can be seen in Figure 3.4.

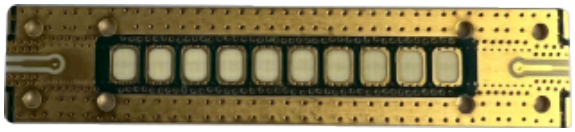

Figure 3.4: Finished design of the PCB.

A dedicated copper package was designed using Fusion 360 in order to house the PCB and the HW structure filled with the AlN dielectric. The package consists of a bottom part at which the hermetically sealed SMA connectors 32K103-5H0L5 from Rosenberger is used. The bottom part and the connectors are then soldered onto the PCB. The filter is enclosed by a top part which has a separate compartment

for the filtering section in order to minimize leakage between port 1 and 2 at high frequencies. In addition, the cavity is filled by the conductive foam Eccosorb® LS-24 to absorb radiation drained by the filter HWs. An exploded view of all the components designed for the package can be seen in Figure 3.5. It should be noted that the HWs has a milling radius of 0.5 mm due to manufacturing constraints. All the mechanical parts, including the dielectric slabs, was manufactured at Chalmers University of Technology at the department of Microtechnology and Nanosience. The resulting size difference compared to the coaxial HERD filter can be seen in Figure 3.6. Comparing the sizes it can be seen that the PCB HERD filter has a reduced size of about 31% for the largest diagonal of 15.8 mm compared to the coaxial HERD diameter of 23 mm (including the absorber). Vertically, it is a decrease of 47% while horizontally, the size is reduced by 57%.

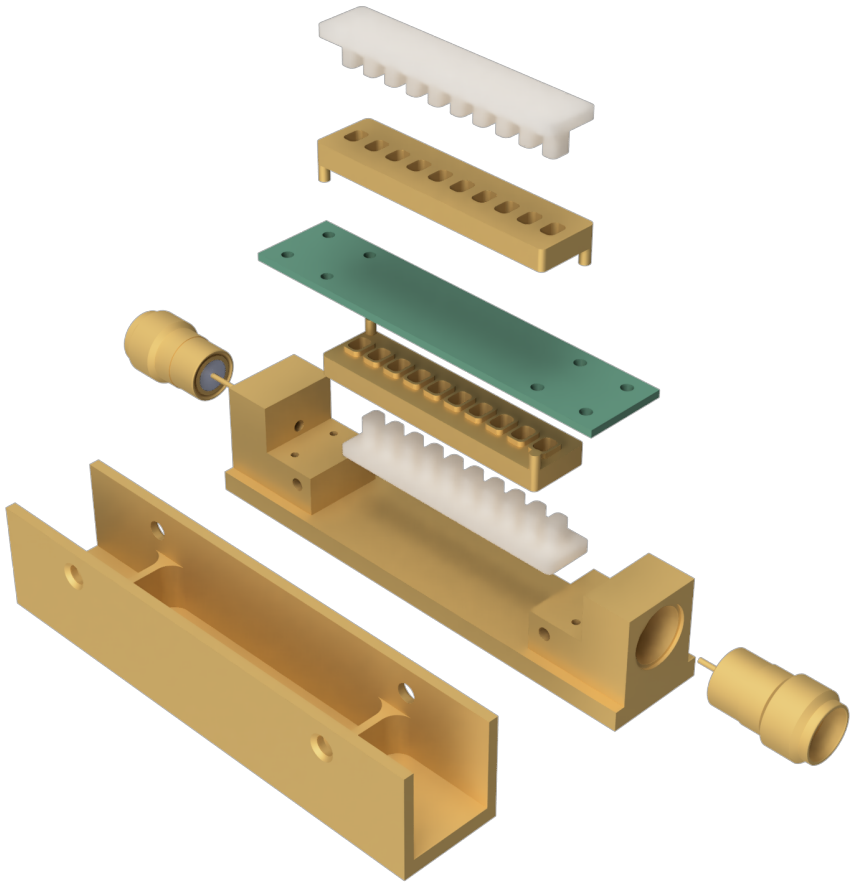

Figure 3.5: Exploded view of the HERD filter implemented in PCB technology with a dedicated package. Note that the screws and absorptive material are left from this image.

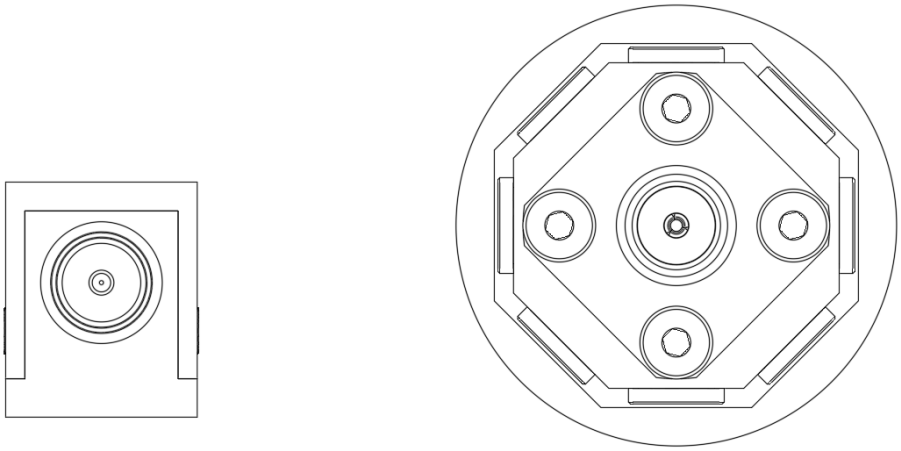

Figure 3.6: Comparison of size between the first version coaxial HERD filter (23 mm diameter) and the PCB HERD filter (15.8 mm diagonal) designed in this thesis.

3.2 Miniaturized Coaxial HERD Filter

As mentioned previously, a viable option for miniaturization is by simply increasing the dielectric constant of the dielectric filament inside the HWs. This will reduce the electrical size according to (2.16). By simulating a model of a coaxial implementation of a HERD filter it was possible to converge on a design which has a total diameter of 9.7 mm of the main body. The same AlN material was used as in the PCB based HERD filter. This resulted in square shaped aperture of size 2.5x2.5 mm. It was also noticed during simulation that the fields does couple much worse than what (2.38) suggests, which allows for a smaller depth of the HWs. For such a small design, the connectors could possibly become the limiting factor. An image of the full design can be seen in Figure 3.7.

Figure 3.7: Implementation of a miniaturized coaxial HERD filter.

3.3 Measurement Setup

The characterization of the filter was performed by measuring the S-parameters with a VNA. This was be done for different frequency ranges. For characterization of the passband in the lower GHz range, the Ceyear 3672A VNA was used. Calibration was performed with the 31121 female Ceyear calibration kit. This measurement was also performed when the filter was submerged in a bath of LN2 (77 K) in order to study

the effects of decreased metal resistivity and mechanical stress on the passband. An overview of the passband measurements can be seen in Figure 3.8.

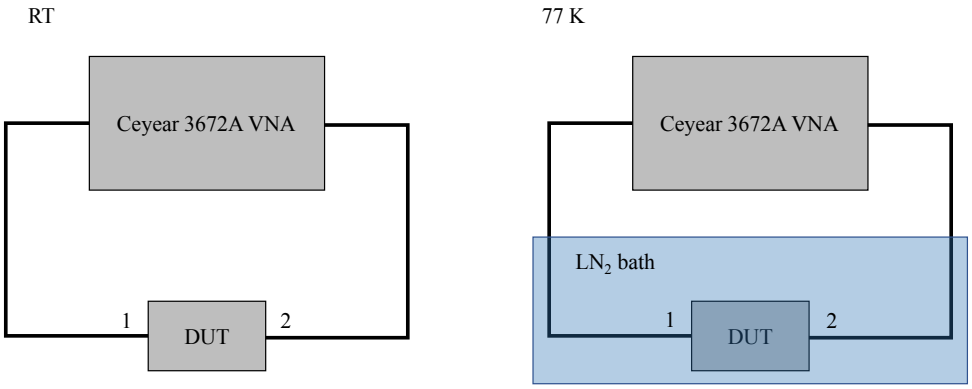

Figure 3.8: Measurement setup for the passband measurements in room temperature and LN2 at 77 K.

For measuring the stopband of the filter, the Anritsu MS4647A VNA with the Anritsu MA25300A mmW Module 145 GHz extensions were used. In order to interface between the 0.8 mm male output of the extenders and the Device Under Test (DUT), several adapters were needed to reach the SMA connectors on the filter. The measurement setup can be seen in Figure 3.9. Calibration was done by performing a through calibration.

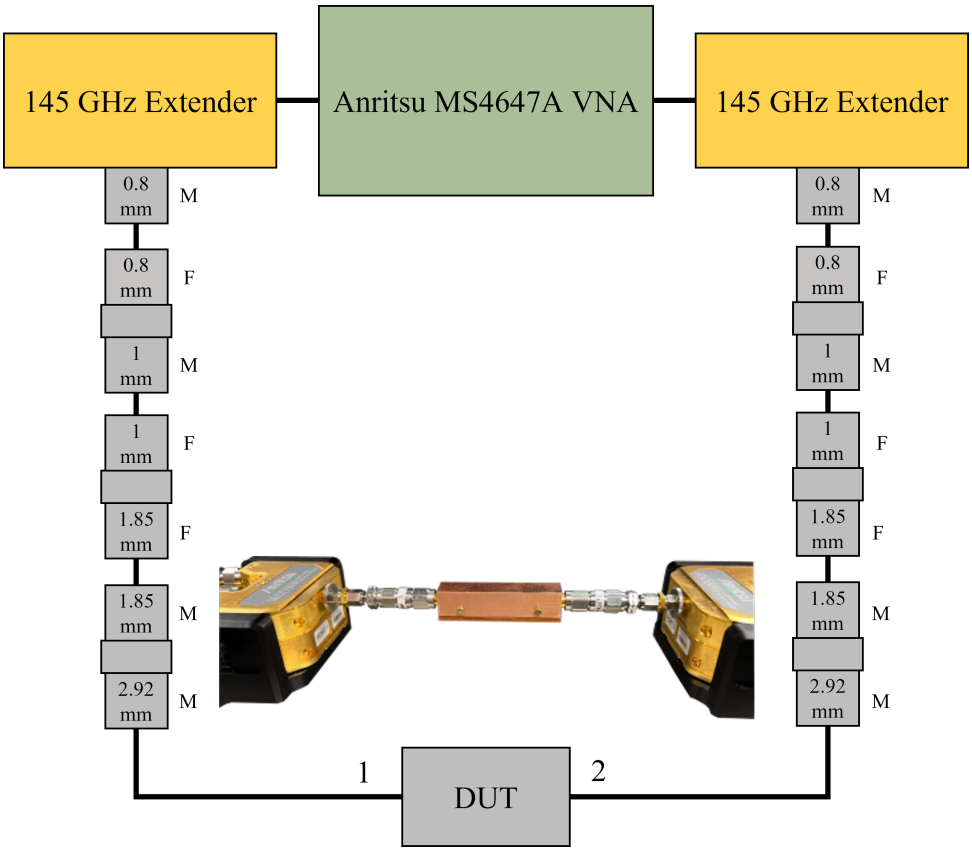

Figure 3.9: Measurement setup for the 145GHz measurement. Here, F/M = Female/Male of the connectors.

An additional measurement was performed by using the Keysight PNA-X VNA to measure the filter up to 67 GHz in room temperature and in LN2 at 77 K. This was done with a similar measurement setup as during the measurements of the passband.

4

Results

In the following chapter the results obtained through Electromagnetic (EM) simulation, measurement and eigenmode decomposition of the PCB HERD filter is presented. In addition, a method of absorbing parasitic substrate radiation in the PCB substrate using absorptive Non Plated Through Hole (NPTH) is presented. Initial simulation results for a miniaturized coaxial HERD filter is also be presented. First, the simulation results of the PCB HERD filter is presented, including the matching structure of the filtering section, CPW to stripline transition and the landing pad for the SMA connector exciting the CPW. In addition, effects of different loss mechanisms on the passband insertion loss is studied. Second, S-parameter measurement of the prototype is presented including data taken at room temperature and at 77 K when the device is submerged liquid nitrogen. In addition, results of the 145 GHz measurement is presented. The results is then compared to the simulation results. After this, the results from the eigenmode decomposition of the HERD HWs is presented for different frequencies. Lastly, simulation results of the miniaturized coaxial HERD filter is presented.

4.1 Simulations

The initial model of the PCB HERD filter described in Chapter 3 had an aperture width of $a = 2$ mm and $b = 1.4$ mm. In order to transform the initial design into a proper device, the device must be matched to 50Ω at every transition and interconnect while still maintaining the desired filter characteristics. In this section, the different simulation results leading up to the finished device is presented. The methods used to perform the simulation is described in Chapter 3.

4.1.1 Stripline Matching Structure

When etching the apertures in the PCB groundplanes, the initial stripline structure simulated in Figure 3.2 becomes highly inductive which can be seen in the smith chart in Figure 4.1. To balance out this inductance, it is possible make the stripline more capacitive by increasing the width of the stripline at the position of the apertures. The results by doing this can be seen in Figure 4.2, where the impedance matching is restored. It can be seen that the matching sections reduce the ripples in passband. Another observation is that the matching slightly improves the attenuation in the stopband, which suggests that the standing wave interference resulting

from the impedance mismatch affects the coupling to the apertures.

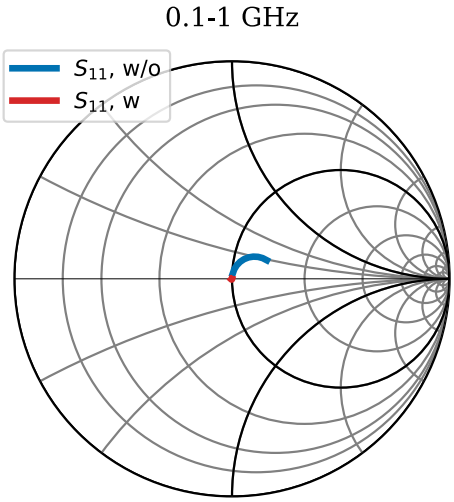

Figure 4.1: S_{11} plotted in a smith chart for low frequencies where the inductive behaviour can be seen without the matching sections. It can be seen that when the matching sections are added, the filter is well matched to 50Ω.

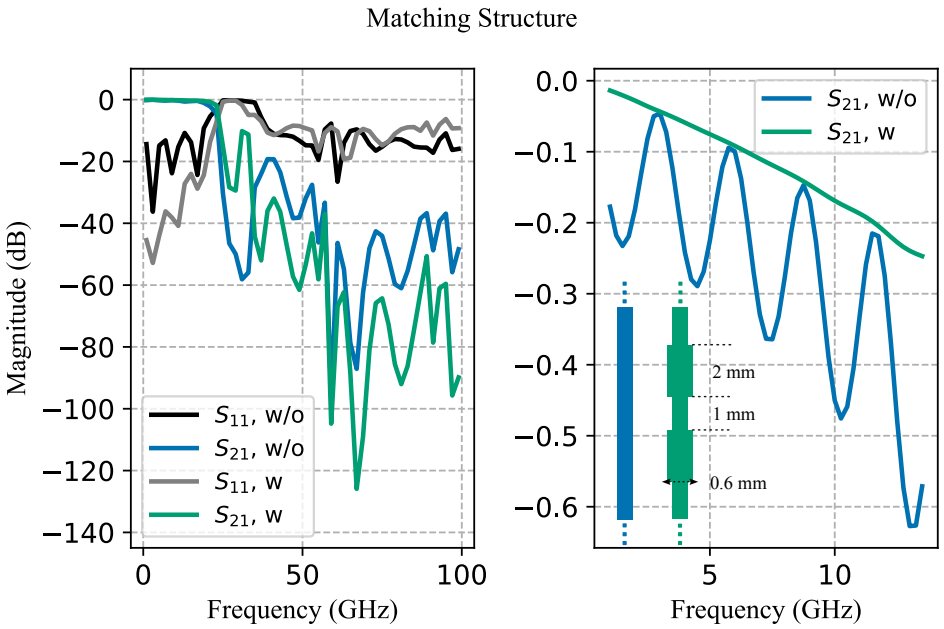

Figure 4.2: Comparison between the stripline with (w) and without (w/o) capacitive sections at the aperture. To the right, S_{11} and S_{21} can be seen from 1-100 GHz. A zoom in on resulting S_{21} can be seen to the left, where the ripples in the passband are reduced.

4.1.2 CPW to Stripline Transition

Given that the transmission lines are embedded within the PCB, the filter requires excitation through an intermediate transmission line, such as a coplanar waveguide (CPW), which is positioned on one of the exposed metal layers. To establish this connection, a via transition must be designed to connect the two transmission lines. The behavior of the via transition can vary depending on its geometry, exhibiting either capacitive or inductive characteristics. Therefore, it is essential to carefully adjust the dimensions around the transition to achieve proper matching. In Figure 4.3, the obtained results are presented, simulated on a model that is excited at the CPW on ports one and two. The via has a radius of 200 μm and a total diameter of the annular ring at 840 μm. The annular ring consists of additional metal surrounding the via hole, which ensures a secure attachment of the via to the copper layer. With these tuned dimensions, the structure remains well-matched across a wide bandwidth.

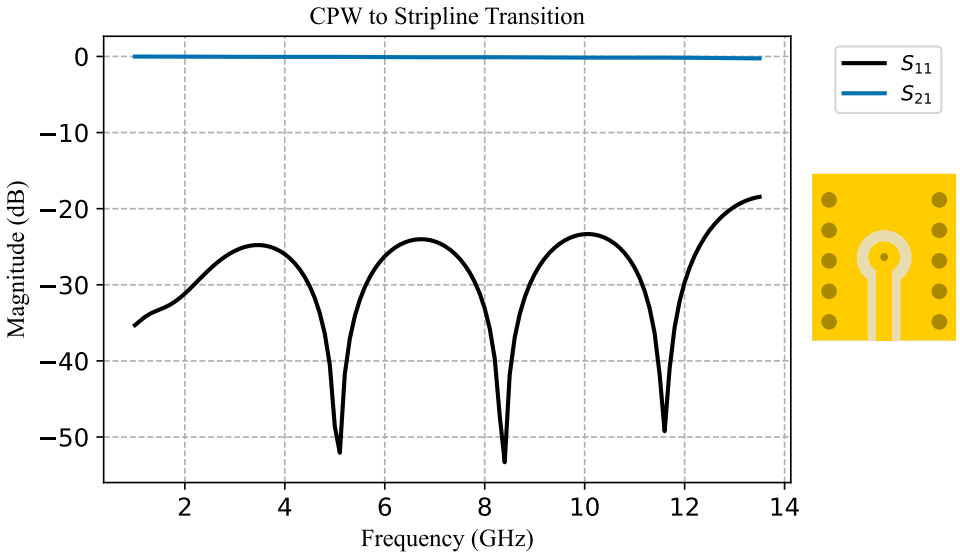

Figure 4.3: Simulation results of the matched CPW to stripline transition. To the right, the tranistion close to the CPW can be seen.

4.1.3 SMA to CPW transition

In order to control the impedance at the transition from the SMA connector to the CPW, a small matching section is added to balance out the added capacitance from the relatively large SMA pin (0.5 mm in diameter) lying on top of the CPW. The results can be seen in Figure 4.5. The simulated model is excited at the connector with a coaxial lumped port at port 1 and 2. A large improvement of the return loss can be seen comparing the results with and without the matching section. It should be noted that in order to achieve good performance of this transition, it is also important that the soldering of the pin is clean so that it resembles the simulated case as close as possible. The dimensions of the transition can be seen in Figure 4.4. It should be noted that the simulation model contains the optimized via transitions

from the previous section.

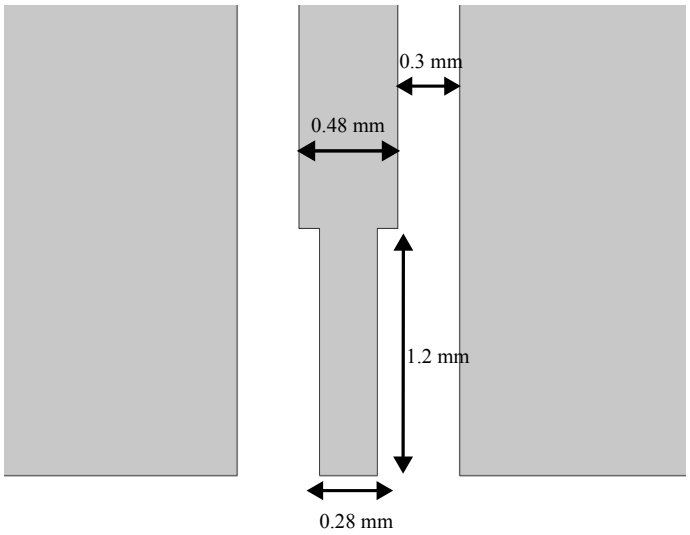

Figure 4.4: Geometry of the SMA excitation on to the CPW.

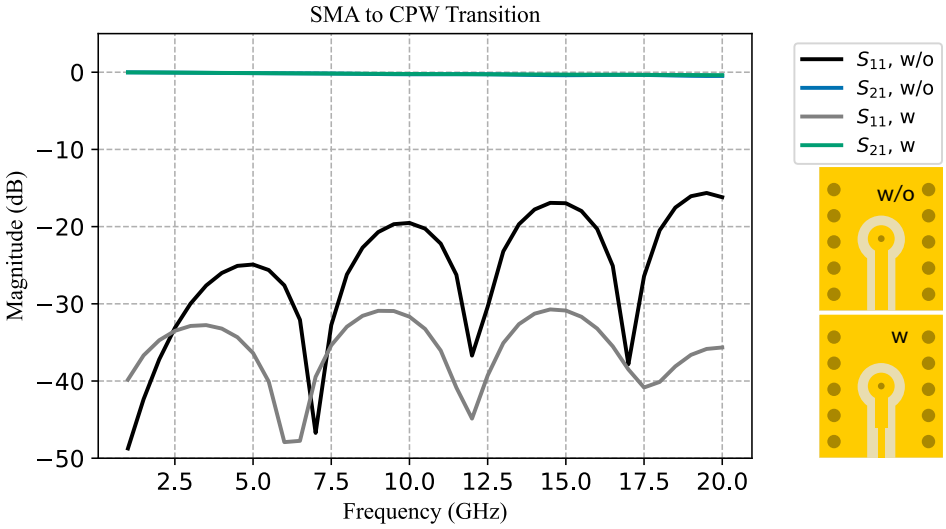

Figure 4.5: Resulting S-parameters by adjusting the landing pad of the SMA connector pin which can be seen in the schematics to the right.

4.1.4 Absorber Termination

In the initial simulations of the PCB HERD filter, the HWs is terminated by SBC. It is interesting to study the performance of the filter model when terminated by a lossy material as described in Section 3.1. The results comparing the simulation when terminated by SBC and an absorber can be seen in Figure 4.6. It can be seen that both methods yield similar results. A sweep of the depth of the HWs is also studied for the absorber termination. This is compared with the insertion loss predicted by the basic loss model in (2.38) and the results can be seen in Figure

4.7. Clearly, the tunneling loss is significantly smaller than what is predicted by the model.

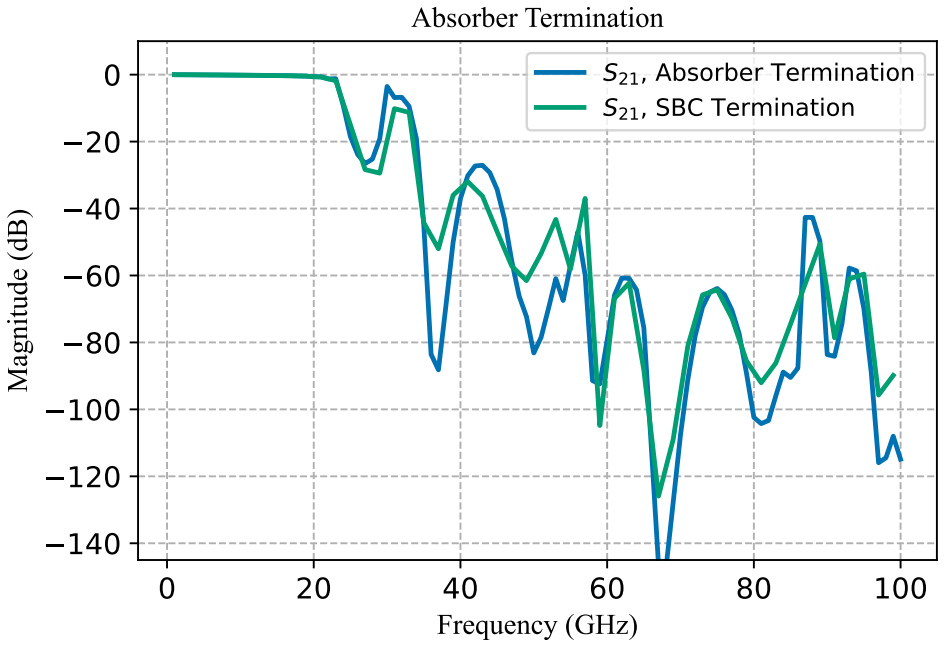

Figure 4.6: Comparison between HWs being terminated with a 1 mm absorber and with SBC.

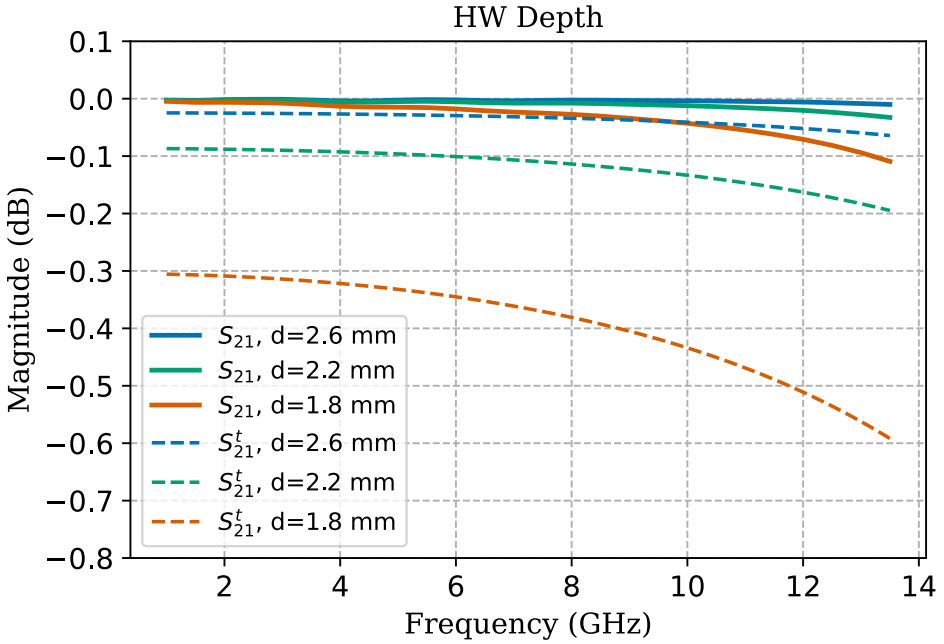

Figure 4.7: Tunneling loss effects on the (solid lines) simulated passband transmission with varying depths of the HWs in comparison to the (dashed lines) theoretical S^t_{21} obtained through the basic loss model described in (2.38).

4.1.5 Full Model Simulation

With all different interconnects added to the filter model, the entire filter structure excited at the CPWs was simulated. To prevent the signal from leaking into the substrate at high frequencies, a via fence is added on both sides of the stripline. In the first simulation of the model including the via fence, a significant increase in transmission in observed starting at about 70 GHz, seen in Figure 4.8. By decreasing the via offset by 200 μm, the behaviour disappears. In the simulation, a large part of the total substrate was removed from the simulation volume in order to reduce simulation time. In order to capture any leakage effects through the PCB substrate, a simulation was performed including the entirety of the PCB with a substrate width $w_{sub} = 8$ mm. From Figure 4.9, it can be seen that the attenuation in the stopband decreases compared to the case when only a minimal part of the PCB substrate is included in the model. This suggests that there is a significant leakage through the substrate, which might be a limiting factor for HERDs filters implemented in planar circuit technologies.

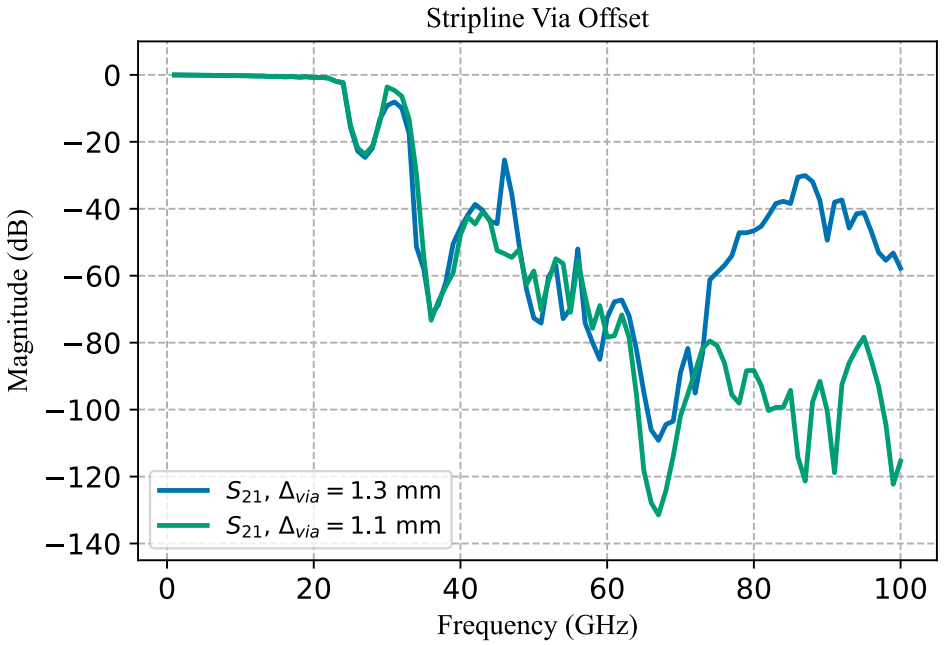

Figure 4.8: Simulation of the filter excited at the CPW with different via offsets Δ_{via}, which is the distance between the stripline and the shielding vias.

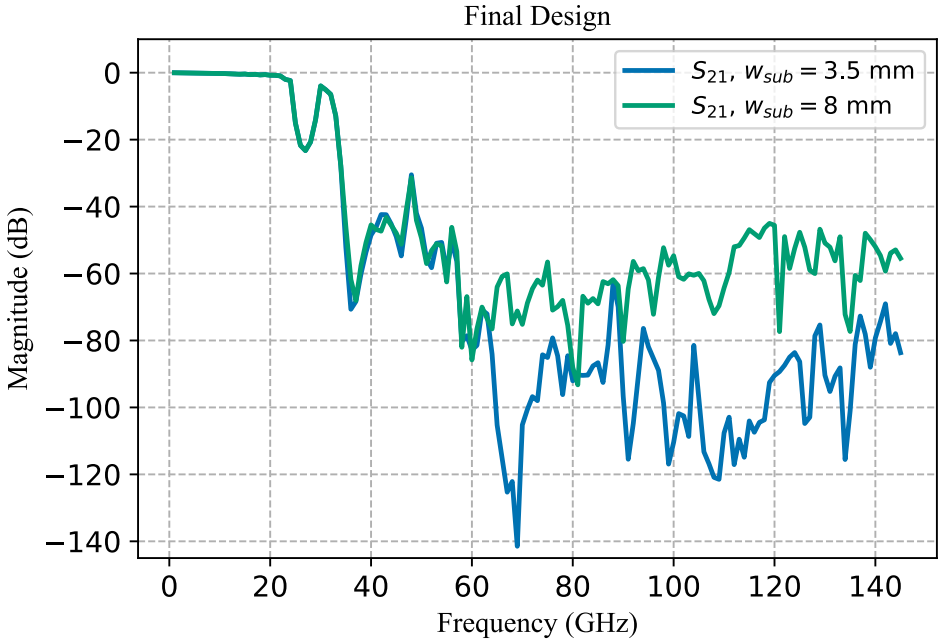

Figure 4.9: The final model simulated with (green) and without (blue) the entire PCB substrate included in the model.

4.1.6 Loss Modelling

Finally, it is also of interest to model the losses coming from a finite conductivity and non smooth conductor surfaces. This was performed using IBC for the conductor boundaries. The copper conductivity at room temperature is taken as $\sigma = 5.813 \cdot 10^7$ S/m [13] and a ENIG conductivity of $\sigma = 10^6$ S/m on top of the CPW based on [29]. The IBC implemented in COMSOL assumes that the currents induced in the metal are pure surface currents where the conductive losses are calculated from the surface conductivity. Hence, Maxwells equation does not need to be solved for the interior of the metal which can save computational resources. This is accurate if the skin depth is much smaller than the size, or thickness, of the conductor.

According to COMSOL [30], using IBC may still be an accurate method of modelling metals if the thickness is at least one order of magnitude larger than the skin depth. At 1 and 10 GHz, the skin depth for room temperature copper is about 2.08 and 0.66 μm respectively which is more than an order of magnitude larger than the thickness of the copper layers at 35 μm. However, for ENIG the skin depth varies between 5.03 and 15.9 μm in this frequency range. Hence, the metals where modelled with copper conductivity only. Based on unpublished results of copper resistivity at cryogenic temperature, the conductivity of RO4350 laminate copper is $\sigma_{77K} = 1. \cdot 10^9$ measurement from Rehammar et al. The surface roughness is entered as specified in the datasheet of RO4350B with $\Delta_{rms} = 3.2$ μm for the inner layer and $\Delta_{rms} = 0.4$ μm for the exposed copper layer. At 77 K, the copper conductivity increase to $\sigma = 5.596 \cdot 10^8$ which was also simulated. The resulting transmission can be seen in Figure 4.10.

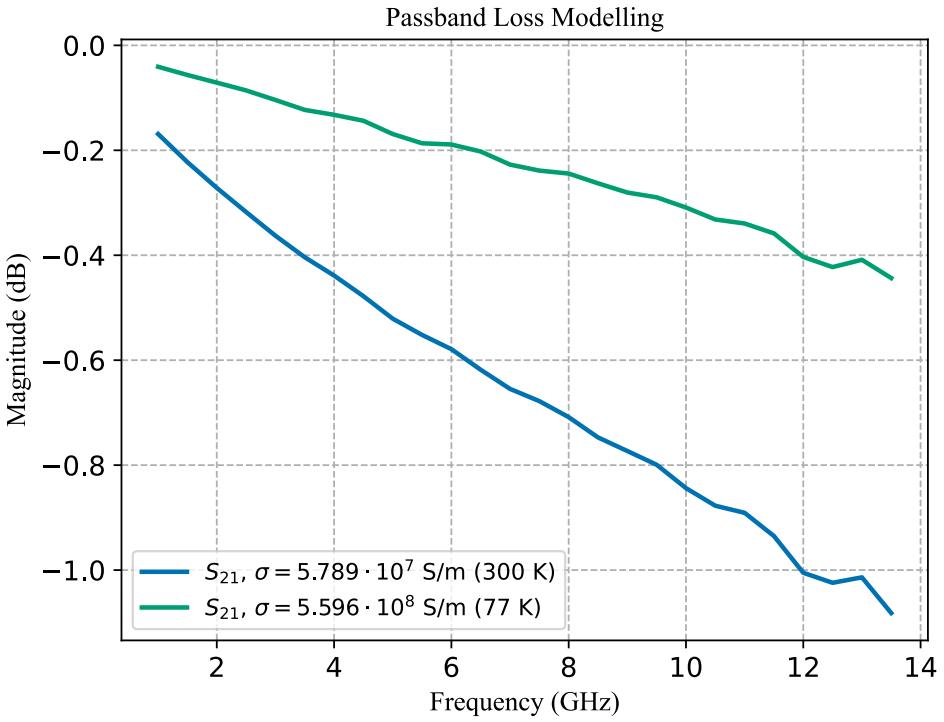

Figure 4.10: Loss modelling of the final filter structure with linear estimates of copper conductivty for room temperature (300 K, blue) and LN2 (77 K, green). Surface roughness of the materials are added in accordance with the datasheet specifications.

4.2 Measurements

4.2.1 Room Temperature Measurements

The first VNA measurement of the PCB HERD filter was performed in room temperature from 10MHz-13.5 GHz using the Ceyear 3672A VNA. Calibration of the VNA was performed using 31121A 3.5mm female Ceyear calibration kit. The measurements was taken with an input power of 0 dBm and an IF bandwidth of 1000 Hz. The results can be seen in Figure 4.11. The filter has a return loss of maximum 16.39 dB in the measured frequency range and insertion loss of 0.76 dB below 8 GHz. The insertion loss corresponding to a return loss of 16.39 dB is $S_{21,\mathrm{dB}} = 20\log_{10} 1 - |S_{11}|^2 = 0.20$ dB. This shows that the filter is not yet limited by return loss in room temperature. It should also be noted that this is the maximum insertion loss resulting from the return loss.

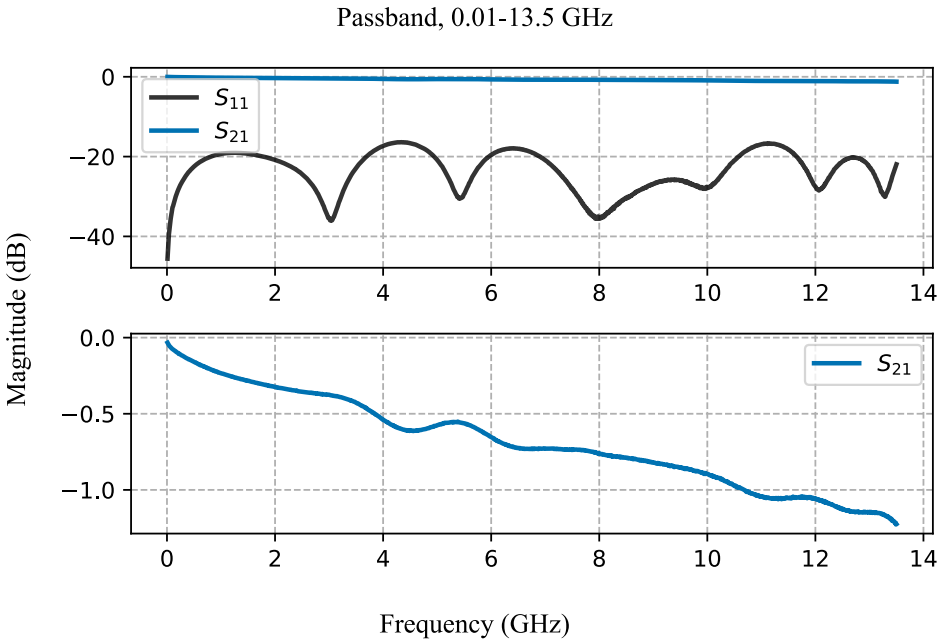

Figure 4.11: Measured S-parameters of PCB HERD filter at room temperature.

To characterize the stopband, the filter was measured in up to 145 GHz using the Anritsu MS4647A VNA with the Anritsu MA25300A mmW Module extensions. The measurement setup is described in Section 3.3. During calibration, signs of overmoding was seen at around 125-130 GHz, which can be seen as an artefact in all the measurements. The IF bandwidth was set to 100 Hz during measurements and the noise floor can be seen in the in Figure 4.13, where the overmoded calibration artefact can be clearly seen. The resulting measurement of S_{21} can be seen in Figure 4.12. The filter has an insertion loss above 40 dB in the stopband above 80 GHz up until around 125 GHz where a peak can be seen. This is ascribed to the overmoding of the thru adapter during calibration.

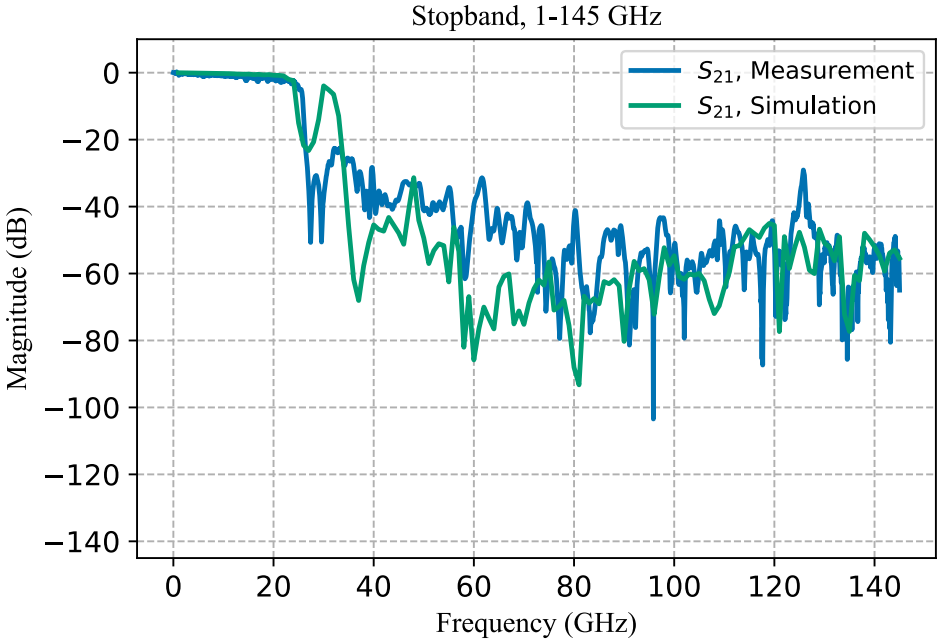

Figure 4.12: S-parameters of PCB HERD filter measured at room temperature up to 145 GHz.

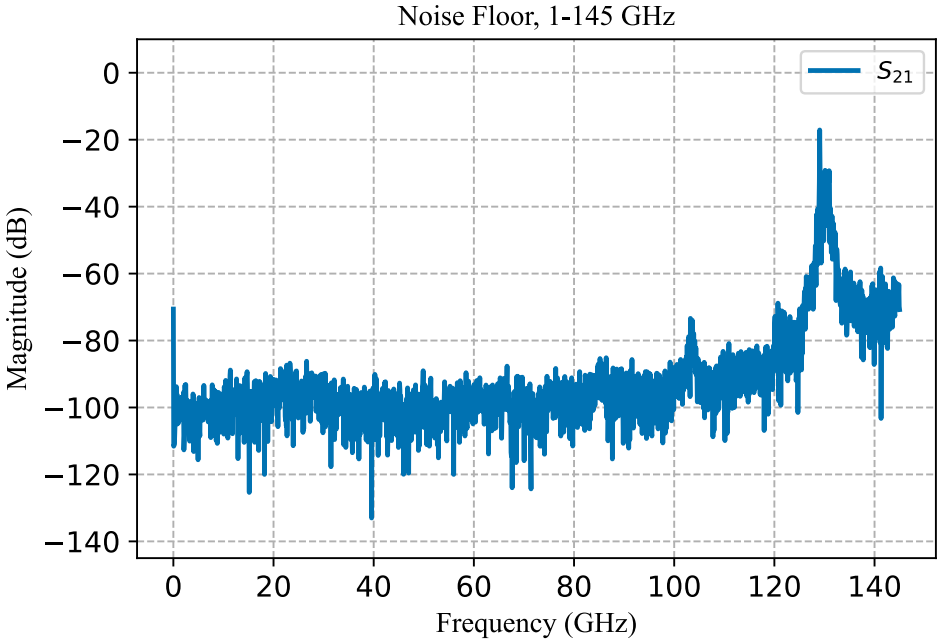

Figure 4.13: Noise floor measurement up to 145 GHz of the Anritsu MS4647A VNA, measured with both ports terminated by a short circuit termination.

4.2.2 Cryogenic Measurements at 77 K

The cryogenic measurements was performed according to the description in Section 3.3. To ensure that the filter was thermalized to the LN2 bath, the data was taken

when the LN2 bath had stopped boiling and the trace of the VNA stabilized. The results of the passband measurements can be seen in Figure 4.14. The magnitude of S_{11} stays below -16.56 dB up to 8 GHz, for which the insertion loss has a maximum of 0.29 dB. The curve showing S_{11} roughly follows the room temperature measurement up until 7 GHz. At around 11 GHz, the return loss deviates from the room temperature measurement and reaches a maximum value of 13.96 dB.

At this temperature, the insertion loss is still dominated by the conductive losses. To illustrate this, the mismatch loss $\mathrm{ML}_{dB} = 10\log_{10} 1 - |S_{11}|^2$ is plotted together with the the magnitude of S_{21} in Figure 4.15. In addition, the difference between the mismatch loss and the magnitude of S_{21} as well as difference between the simulated insertion and mismatch loss is also visible. The insertion loss is clearly dominated by the conductive losses with good agreement between simulation and measurements at 77K. This suggests that modelling conductive losses with IBC for PCBs at cryogenic temperatures can provide good knowledge about what losses to be expected. In room temperature, this seems to not be the case which could be antributed to that ENIG was not included in the simulations.

The filter was also measured up to 67 GHz in room temperature as well as in a LN2 bath, for which the results can be seen in Figure 4.16. As for the passband measurements, the data was taken when the LN2 stopped boiling. Only small differences can be observed between both cases, which indicates that the filtering characteristics does not change much at cryogenic temperatures.

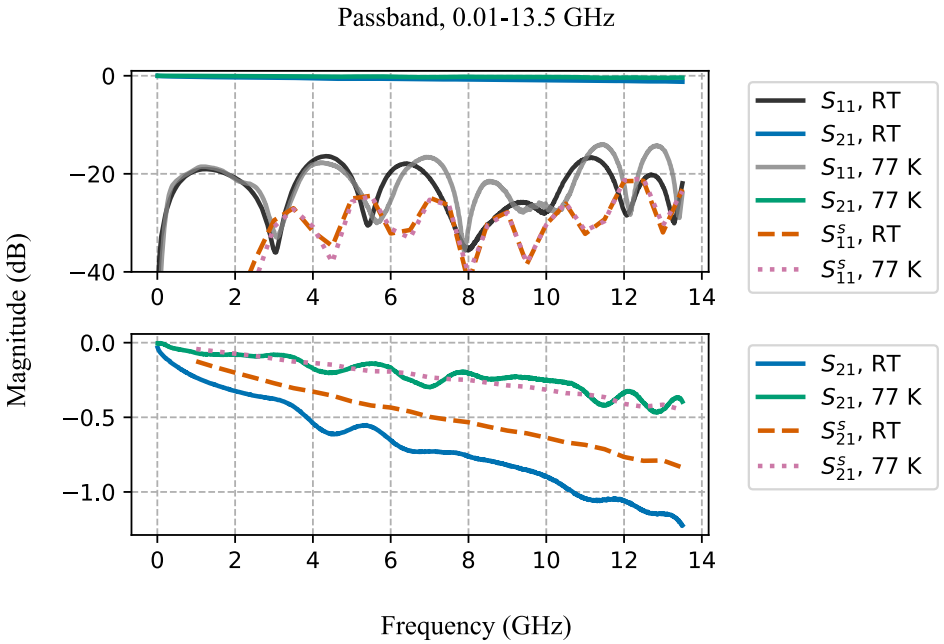

Figure 4.14: (solid lines) S-parameters of the passband when submerged in 77 K liquid nitrogen compared with room temperature measurements together with (dashed and dotted lines) the simulations containing finite conductivity and surface roughness.

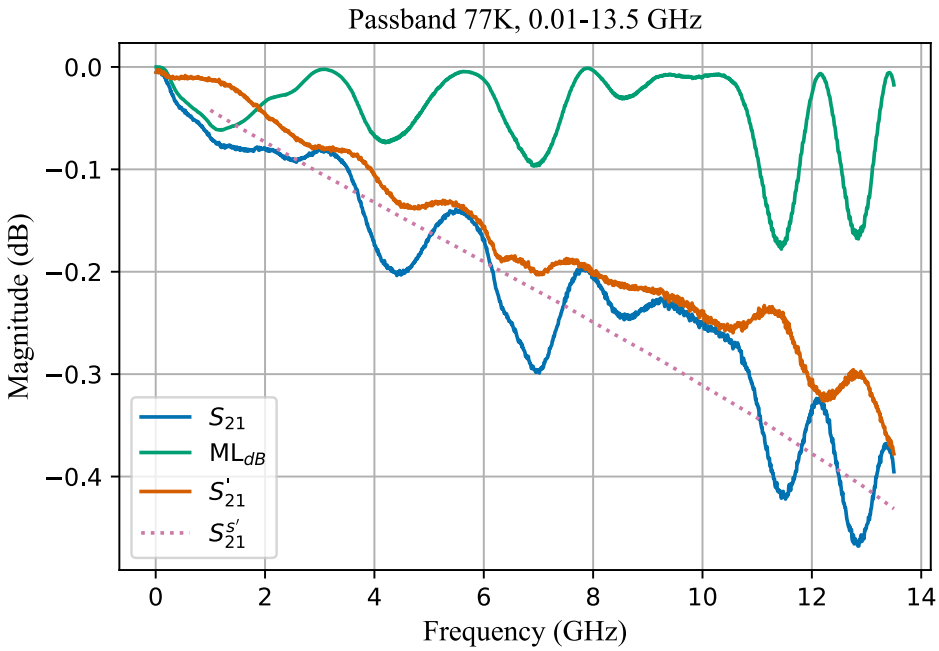

Figure 4.15: Zoom in on the magnitude of S_{21} measured at 77K compared to the mismatch loss ML_{dB} and the simulated insertion loss using IBC.

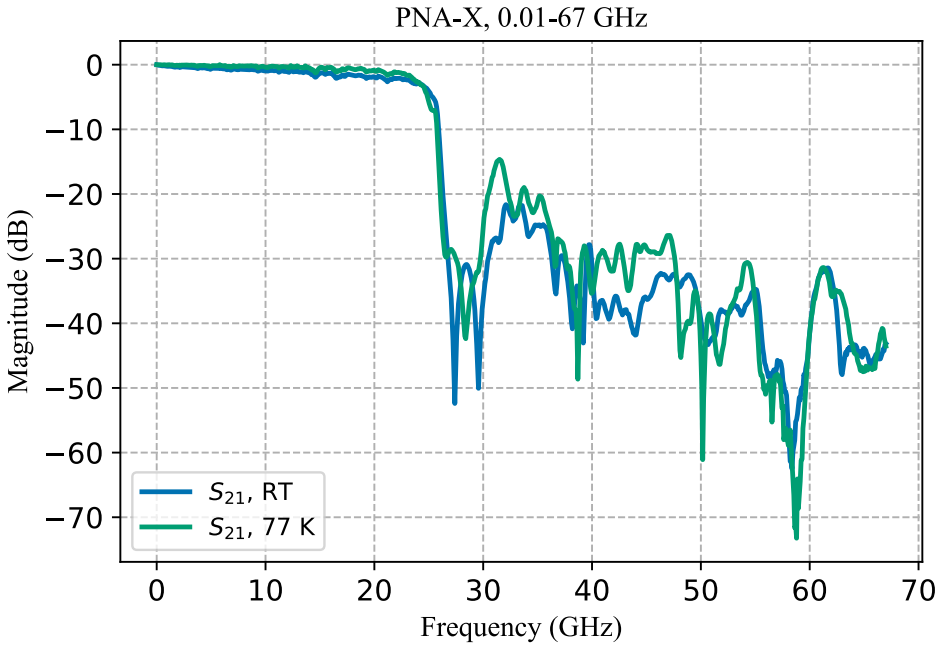

Figure 4.16: S-parameters of the passband when submerged in 77 K liquid nitrogen compared with roomtemperature measurements.

4.3 Non Plated Through Hole Substrate Integrated Absobers

During simulations, an interesting observation was made regarding the leakage through the PCB substrate, which was found to decrease the level of attenuation in the stopband. This effect can be seen in Figure 4.17. To address this issue, a potential solution is to incorporate NPTH filled with a lossy material. These NPTH absorbers serve the purpose of absorbing radiation that escapes the main propagation path (the stripline). In order to evaluate the impact of these absorbers, the same model used to simulate the final design structure, including the NPTH absorbers, was simulated up to a frequency of 130 GHz. The simulation results, depicted in Figure 4.18, clearly demonstrates the effectiveness of employing NPTH absorbers. The attenuation achieved with their presence is significantly higher compared to the scenario where they are not utilized. Interestingly, the discrepancy between the two cases becomes noticeable above 60 GHz. This suggests that the substrate leakage begins to exhibit a substantial influence around this frequency.

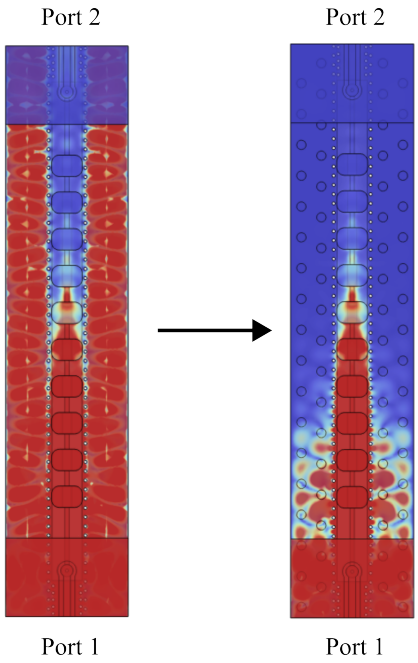

Figure 4.17: Comparison between norm of the electric field distribution with and without the NPTH absorbers at 78 GHz. The NPTH can be seen as circles in the substrate in the field overlay to the right.

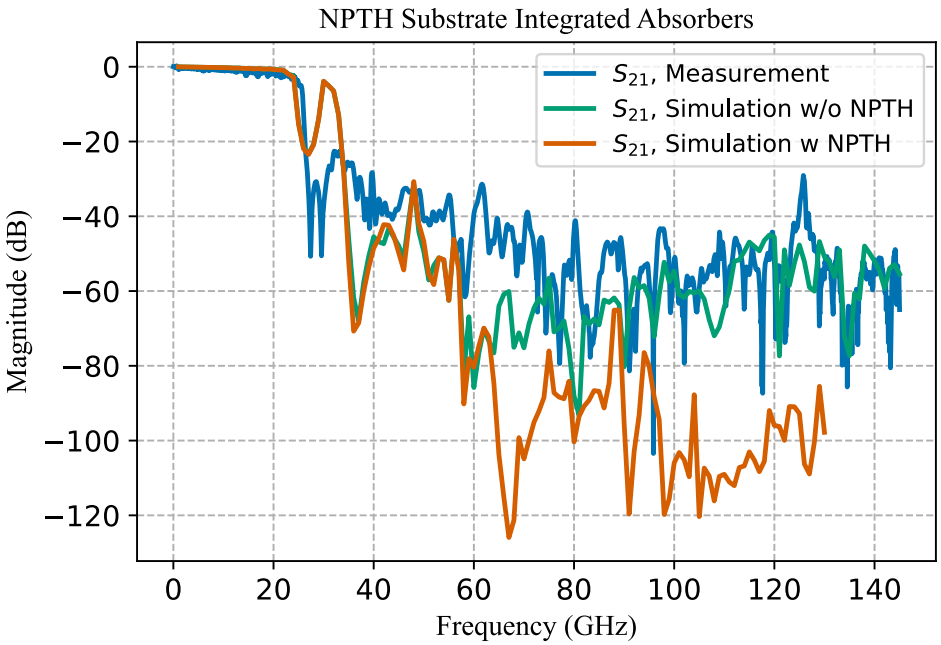

Figure 4.18: 145 GHz S-parameters in comparison with the simulated NPTH absorber model.

4.4 Field Decomposition of HERD Apertures

In this section the results of the field decomposition inside the PCB HERD apertures is presented. The electric field is extracted in a cross section of the HWs obtained from a two-port simulation of a simplified model of the PCB HERD filter, with perfect rectangular HWs in order for the fields to take the form of (2.21)-(2.23) and (2.28)-(2.31). The depths of the HWs are increased to 10 mm in order to analyze the field further away from the aperture to reduce the effects of evanescent fields.

To study if evanescent fields affect the result of the decomposition, the field is extracted at both 1 mm and 5 mm above the aperture at the first HW. This is done at 65 GHz, for which the number of propagating eigenmodes are N=5. In Figure 4.19, both the real and imaginary parts of the fields are plotted against each other when extracted 1 mm above the aperture. It can be seen that some of the components are slightly blurry, although the main profile is seen to be captured in the reconstructed fields. The resulting mode content can be seen in Figure 4.20, where it can be seen that the field content consists of the TE_{10}, TE_{11} and the TM_{11} mode with corresponding $|c_n|^2$ of 0.373, 0.352 and 0.274 respectively. The correlation between the simulated and reconstructed intensities is found to be 0.998.

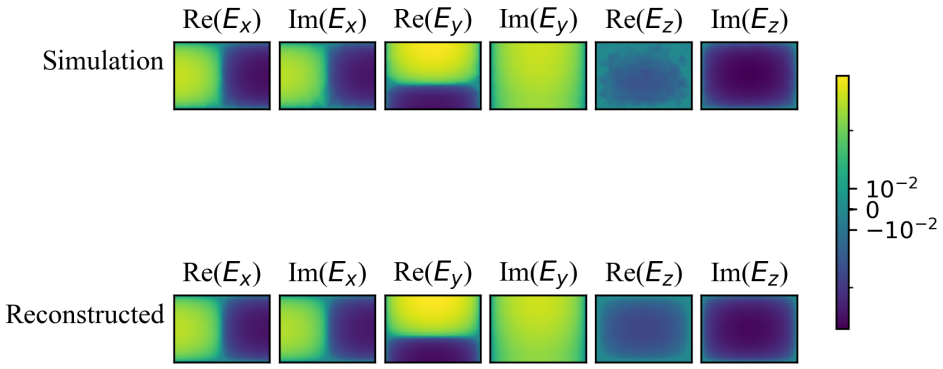

Figure 4.19: The decomposed electric field at 65 GHz, 1 mm above the aperture. As can be seen, some of the vector components of the simulated field are slightly blurry. The amplitudes in the plot are in logarithmic scale.

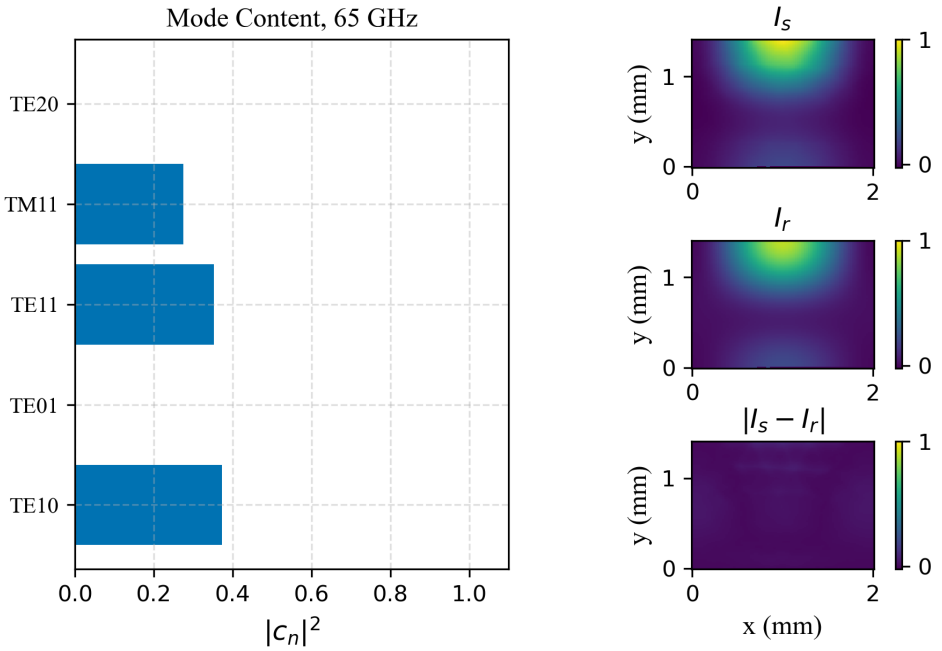

Figure 4.20: Mode content of the electromagnetic field at 65 GHz together with the intensities for the simulated and reconstructed fields in comparison with the discrepancy between the two.

The resulting electric field components when the field is extracted 5 mm above the aperture can be seen in Figure 4.21. Again, some of the field components are slightly blurry in the simulated field. As in the 1 mm case, the mode content is dominated by the TE_{10}, TE_{11} and the TM_{11} modes which can be seen in Figure 4.22. The obtained $|c_n|^2$ for this case was found to be 0.366, 0.361 and 0.273 respectively, which is roughly the same as for 1 mm above the aperture. The intensity correlation for this case is C=0.999.

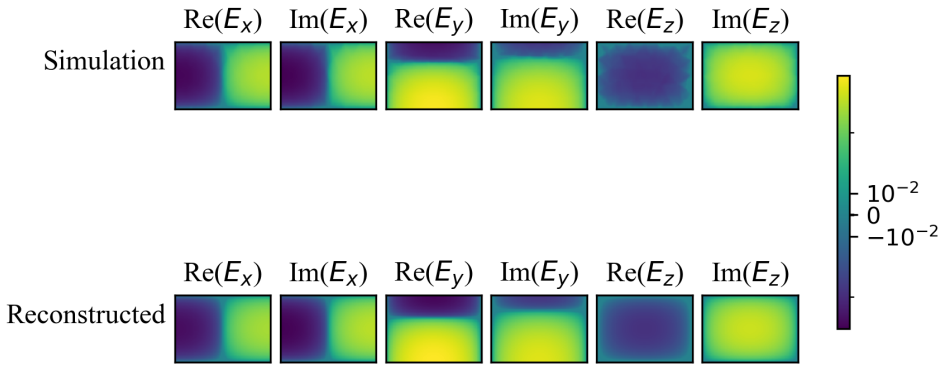

Figure 4.21: The electric field components obtained at a distance of 5 mm from the aperture at 65 GHz.

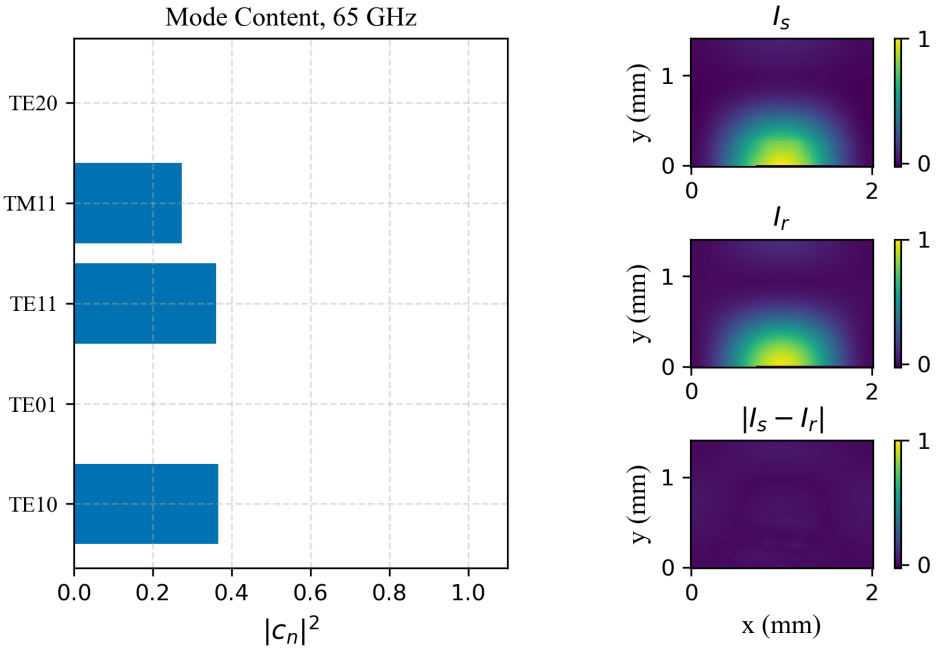

Figure 4.22: The mode content 5 mm above the aperture along with the simulated and reconstructed intensities.

To see how the mode content changes with frequency, the decomposition of the fields are performed at 85 and 105 GHz, both at a distance of 5 mm from the aperture. At 85 GHz, the number of modes propagating inside the HW is N=8. The field components can be seen in Figure 4.23 with good agreement between simulated and reconstructed fields. The mode content can be seen in Figure 4.24, consisting solely of TE_{10}, TE_{11} and the TM_{11} mode with corresponding $|c_n|^2$ of 0.191, 0.197 and 0.613. The correlation between the intensities are C=0.999.

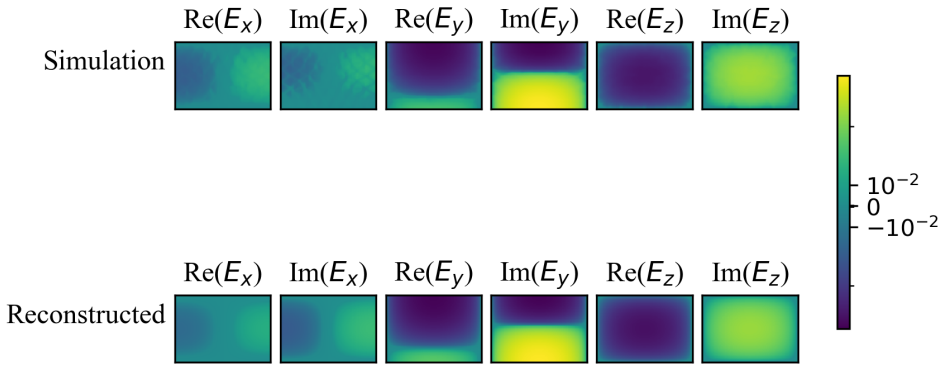

Figure 4.23: The electric field components at 85 GHz.

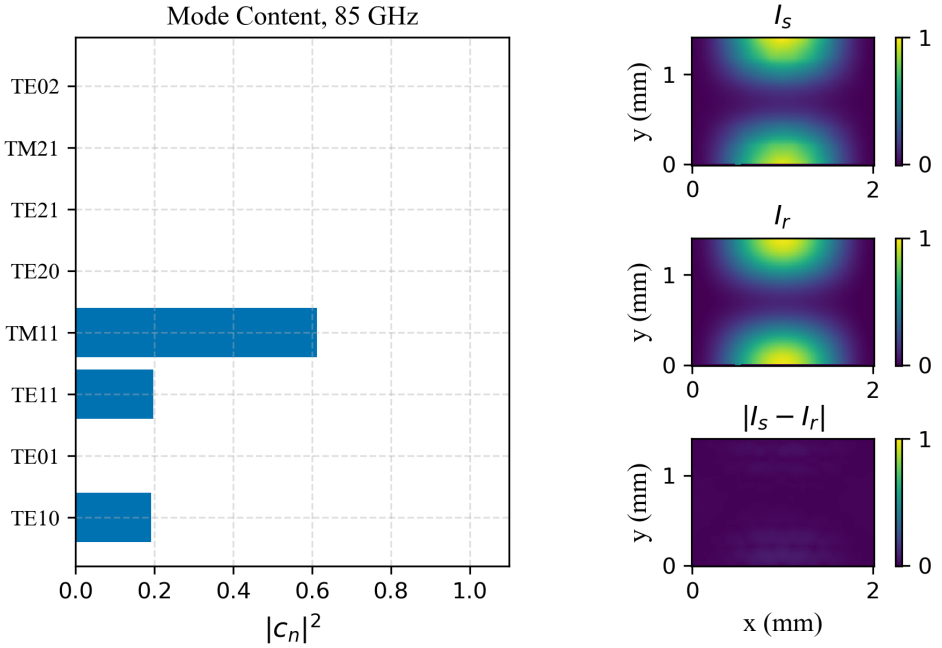

Figure 4.24: The decomposition result at 85 GHz together with the simulated and reconstructed intensities along with their discrepancy.

At 105 GHz, there are a total of N=13 propagating modes that can exist in the HW. The field components can be seen in Figure 4.25 and the mode content can be seen in Figure 4.26 an intensity correlation of C=0.985. At this frequency, the HW is heavily overmoded. The overall results from the decomposition are summarized in Table 4.1. Interestingly, close to the cutoff frequency of the HW the field couples strong the the fundamental TE_{10} mode, but also the two degenerate TE_{11} and TM_{11}. This may suggest that, in order to achieve a sharper cutoff frequency of the filter, the cutoff frequencies of the TE_{11} and TM_{11} should be lowered. A summary of the complex amplitudes obtained for the different frequencies can be seen in Figure 4.27.

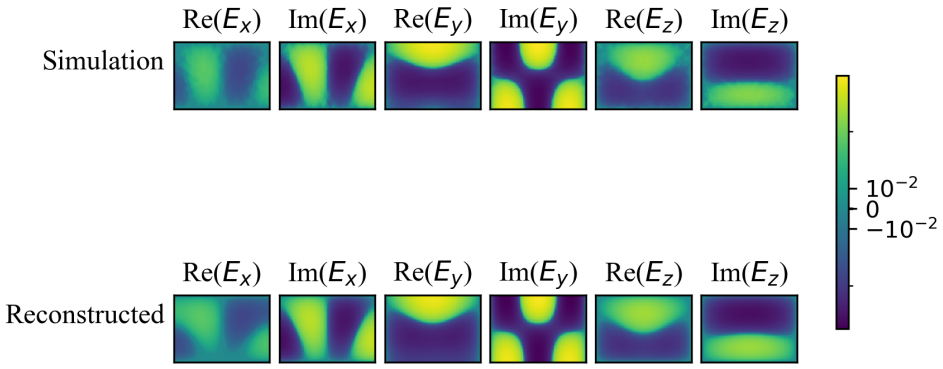

Figure 4.25: The electric fields components at 105 GHz.

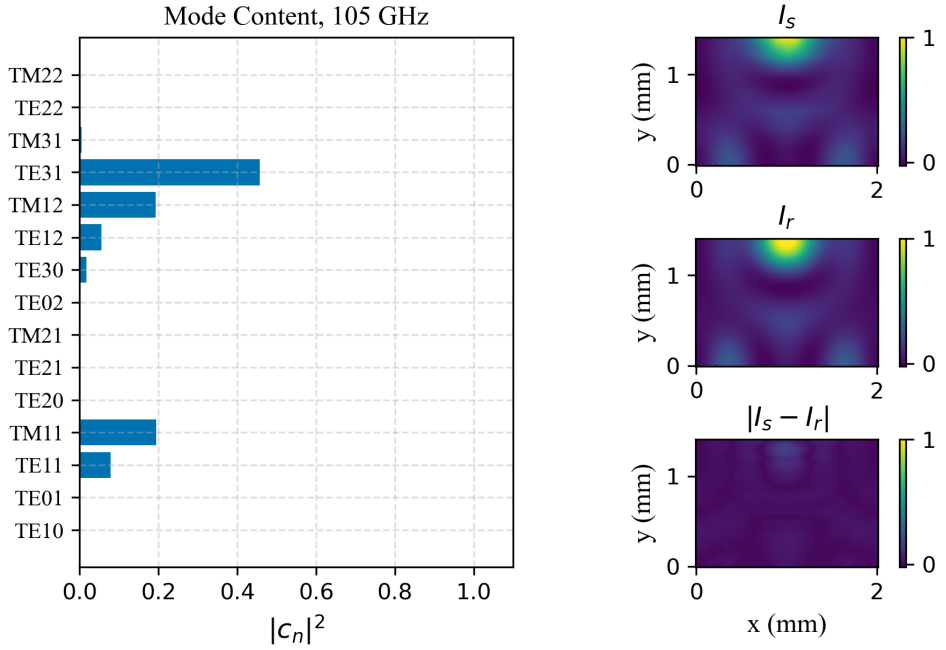

Figure 4.26: The decomposition result at 105 GHz together with the simulated and reconstructed intensities along with their discrepancy.

Summary of Field Decomposition			
Frequency (GHz)	Δ_a (mm)	Correlation (2.44)	$\lvert c_n \rvert^2$
65	1	0.998	TE_{10}: 0.373 TE_{11}: 0.352 TM_{11}: 0.274
65	5	0.999	TE_{10}: 0.366 TE_{11}: 0.361 TM_{11}: 0.273
85	5	0.999	TE_{10}: 0.191 TE_{11}: 0.196 TM_{11}: 0.613
105	5	0.985	TE_{10}: 0.002 TE_{11}: 0.079 TM_{11}: 0.195 TE_{30}: 0.017 TE_{12}: 0.055 TM_{12}: 0.192 TE_{31}: 0.456 TM_{31}: 0.004

Table 4.1: A table summarising the results of the field decomposition of the PCB HERD HWs. The variable Δ_a is the distance above the aperture where the field data was extracted.

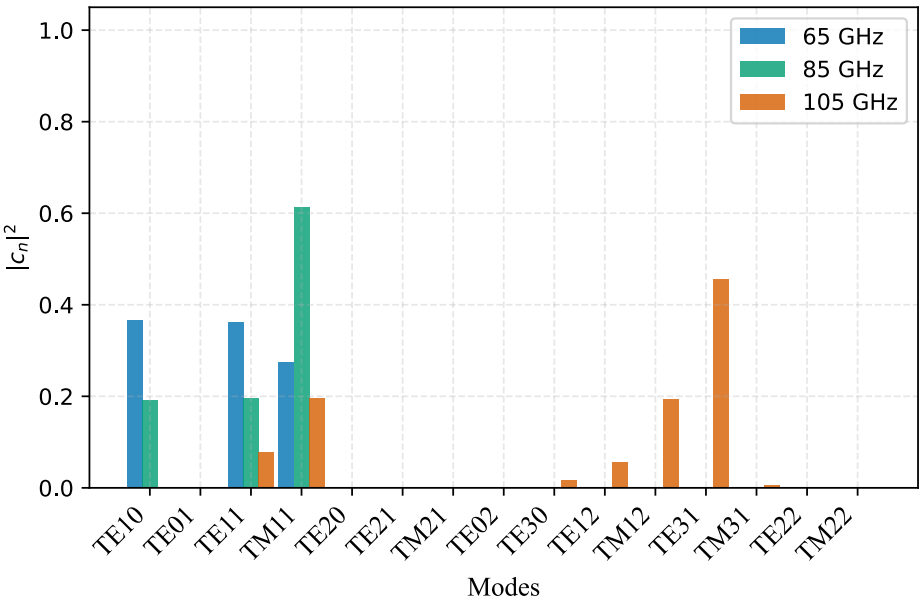

Figure 4.27: Summary of complex amplitudes obtained for different frequencies.

4.5 Miniaturized Coaxial HERD Filter

During the field decomposition study of the PCB HERD filter, it was noticed that the stripline couples strongly to the TE_{10}, TE_{11} and the TM_{11}. This suggests, that in order to have a sharper cutoff frequency of the filter, the cutoff frequency of the TM modes should be designed to be as low as possible for a given fundamental mode cutoff frequency. It was also noticed that the fields couple significantly less than whats predicted by (2.38) which also opens up for further minimization through a decreased depth of the HWs. In Figure 4.28, the S-parameters of a coaxial HERD filter is shown. Here, the fundamental mode cutoff frequency of the aperture is fixed for all aperture dimensions of the simulated model. It can be seen that the cutoff of the filter depends very little on changes of the height b, while changing the width affects the cutoff drastically. The filter has the most attenuation for when the model has square shaped apertures with $a = b = 2.5$ mm. The HWs has a depth of 1.7 mm, arranged in an array of five unit cells of four HWs. The diameter of the filters main body is 9.7 mm, which can be compared to the coaxial filter in [10], which is 18.4 mm in diameter (absorber not included) and has a HW depth of 5.05 mm.

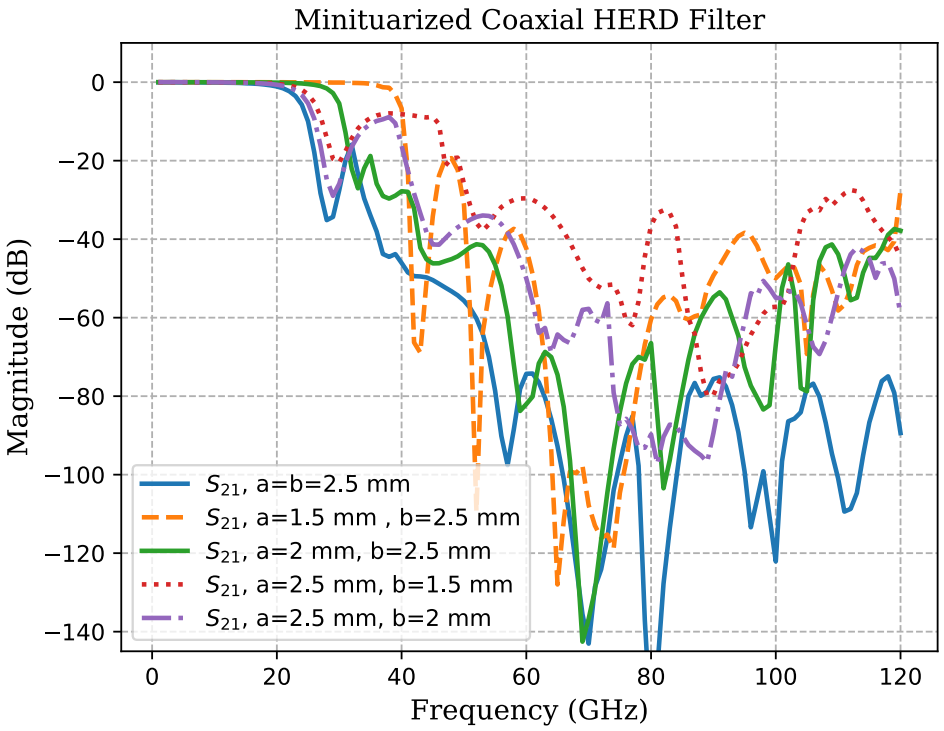

Figure 4.28: Simulation of a miniaturized coaxial HERD filter with square apertures compared to different dimensions of the aperture but with the same fundamental mode cutoff frequency.

5

Conclusion

In the following section, the results presented in Chapter 4 will be summarized and discussed. First the simulation and measurement results will be compared and deviations will be discussed. This will be followed by a summary of the results of the field decomposition which will be discussed in relation to better filter design. The chapter will end with an outlook of future HERD filter development.

5.1 Conclusions

The aim of this thesis was to design a miniaturized HERD filter. To do this, the filter was implemented in PCB technology. Initial simulations of the isolated filtering structure performed in COMSOL Multiphysics showed promising results. This was followed by the design of a CPW to stripline tranistion in order for the filter to connect to a regular SMA connector. The landing pad of the SMA connector pin was designed in order to minimize the effects of the added parasitic capacitance coming from the SMA pin. Finally, a full model of the filter excited at the CPW was simulated.

After the different parts of the filter was manufactured and assembled, the filter was characterized through S-parameter measurements using a VNA. First, the passband was measured between 0.01-13.5 GHz in room temperature. The maximum insertion loss below 8 GHz was measured to 0.76 dB with a maximum return loss of 16.39 dB. This is slightly more loss than what was simulated using only room temperature copper conductivity, which is attributed to the the ENIG plating which was not included in the simulation. During soldering of the hermetically sealed SMA connectors, a slight misalignment of the connectors was noticed, which could be a reason for the decrease of return loss compared to the simulated results. This could be fixed by adjusting the tolerances of the SMA socket in the bottom part of the filter package. This should allow for a more precise alignment during assembly and minimize movement during soldering. It should also be noted that despite the optimized landing pad for the SMA pin, the quality of the soldering job is important to achieve a similar situation of that in the simulation model. To understand this better, one need to assemble and measure more filters in order to see what variations to be expected.

During simulation of the full filter model, it was noted that the via offset, Δ_{via}, seems to have a significant effect on the attenuation at high frequencies. One reason

for this could be that higher order modes excited in the stripline structure couple weaker to the HWs. This could be attributed to factors such as a more diluted field around the aperture where the field distribution is not concentrated primarily at the aperture. No effects of this was seen in measurements, but having the via offset as small as possible seems to be advantageous. It was also notice that leakage through the PCB substrate bypasses the filtering structure, which could be a limitation for the HERD filters implemented in planar circuits. A possible solution for this was presented, using conventional NPTH filled with absorptive material. Simulations show that this strategy is effective in absorbing leakage in the PCB substrate. It should be noted that other leakage paths could exist in the filter, such as between the two ports inside the package. These paths has not yet been investigated.

During measurements of the filter at 77 K it was seen that the maximum insertion loss below 8 GHz was 0.29 dB, which is a decrease of 0.47 dB compared to the room temperature case. The measurements show a similar trend as in simulation, suggesting that modeling metallic losses using IBC is an accurate method to estimate conductor losses at low temperatures. It could also be expected that the resistivity of copper drops slightly more at 10 mK and that the losses therefore can be expected to be smaller when operating at those temperatures inside the cryostat. Also, choosing gold plating instead of ENIG could potentially decrease conductive losses of the filter. It should also be noted that the change in return loss at 77 K is small compared to the room temperature, with smaller discrepancy at frequencies above 8 GHz. In addition, comparing to the measurements performed up to 67 GHz it can be seen that the the filter characteristics change very little at cold temperatures.

Another important observation was made during simulations of the HW depth, it was noted that the filter couples much worse to the apertures than what is suggested in (2.38). This means that the it should be possible to further reduce the size of the filter without affecting performance in the passband. During the same simulations, it was also seen that the scattering boundary conditions used to terminated the HWs produces similar results as when they are terminated by a lossy material.

In this thesis, a tool for analyzing the field content inside the HERD filter structure was developed. Analyzing the PCB HERD filter showed that the HWs becomes highly overmoded far up in the stopband as previously suspected, and that the stripline couples strongest to the TE_{10}, TE_{11} and the TM_{11} mode at lower frequencies. A more systematic study of the frequency dependence of the complex coeffiecient would also be of interest. This is, however, more of a functionality upgrade in order to automatically load data directly from COMSOL instead of manually storing the data, which was done during this study.

The results obtained from the simulations of the miniaturized PCB HERD together with the results obtained from the eigenmode field decomposition, a miniaturized coaxial HERD filter was designed. This design uses the same dielectric filling as in the PCB HERD case and has a reduced size of 43% compared to its predecessor. A model was simulated which showed promising results but was not manufactured and measured during this thesis.

5.2 Outlook

From the insights gained during this thesis, many interesting ideas suitable for further study have become apparent. First off, it would be highly interesting to further reduce the size of the filter, since this has been showed to be possible. This will be required if the filters shall be used in high density qubit systems where high density cabling is needed. Another aspect would be to try new materials and possible other technologies like LTCC technology. This could potentially further reduce both size and conductive losses of the filter. The package of the filter can be improved, both in terms of size but also in terms of improved internal shielding between the two ports.

Another aspect of implementing a HERD filter in PCB technology is that it opens up for integration of lumped surface mount components which can be soldered on to the PCB. Hence, RLC components could be integrated in combination with the HERD filtering technology to create low cutoff frequency filters in the MHz range, which could replace other low cutoff frequency filters which do not have high frequency blocking capabilities.

Next, it would be interesting to realize the NPTH absorbers in the PCB substrate. To do this, one would need to investigate different absorptive materials. A possible implementation would be to fill the holes with a curable absorber, which can be dispensed in an efficient way. Machinable absorptive material are also available such as Laird MF-190, used in one of the simulations in this thesis. In relation to this, it would be interesting to study if NPTH absorbers could themselves work as a lowpass filter for which radiation leaks out and becomes absorbed into the substrate at high frequencies.

Another option would be to decrease the total width of the PCB, similar to the substrate width of 3.5 mm in the model simulated in Figure 4.9. This would also have a positive effect on size, since this would reduce the with several millimeters in horizontally. In order to utilize the full size decrease of the filtering structure, it is also likely that other connector types that SMA must be used in order for the connectors to not become the limiting factor in the size reduction of future HERD filters.

Bibliography

[1] M. Devoret and R. Schoelkopf, "Superconducting circuits for quantum information: An outlook.," *Science*, vol. 339, no. 6124, p. 1169, 2013, ISSN: 0036-8075.

[2] T. Van Duzer and C. W. Turner, *Principles of superconductive devices and circuits.* Prentice Hall PTR, 1999, ISBN: 0132627426.

[3] J. Bardin, D. Sank, O. Naaman, and E. Jeffrey, "Quantum computing: An introduction for microwave engineers.," *IEEE Microwave Magazine, Microwave Magazine, IEEE, IEEE Microwave*, vol. 21, no. 8, pp. 24–44, 2020, ISSN: 1527-3342.

[4] P. Krantz, M. Kjaergaard, F. Yan, T. P. Orlando, S. Gustavsson, and W. D. Oliver, "A quantum engineer's guide to superconducting qubits.," Jun. 2019.

[5] J. M. Martinis, M. Ansmann, and J. Aumentado, "Energy decay in superconducting josephson-junction qubits from nonequilibrium quasiparticle excitations," *Phys. Rev. Lett.*, vol. 103, p. 097 002, 9 Aug. 2009. DOI: 10.1103/PhysRevLett.103.097002.

[6] K. Serniak, M. Hays, G. de Lange, *et al.*, "Hot nonequilibrium quasiparticles in transmon qubits," *Phys. Rev. Lett.*, vol. 121, p. 157 701, 15 Oct. 2018. DOI: 10.1103/PhysRevLett.121.157701.

[7] R. T. Gordon, C. E. Murray, C. Kurter, *et al.*, "Environmental radiation impact on lifetimes and quasiparticle tunneling rates of fixed-frequency transmon qubits," *Applied Physics Letters*, vol. 120, no. 7, Feb. 2022, 074002, ISSN: 0003-6951. DOI: 10.1063/5.0078785.

[8] D. H. Slichter, O. Naaman, and I. Siddiqi, "Millikelvin thermal and electrical performance of lossy transmission line filters," *Applied Physics Letters*, vol. 94, no. 19, May 2009, 192508, ISSN: 0003-6951. DOI: 10.1063/1.3133362.

[9] S. Krinner, S. Storz, P. Kurpiers, *et al.*, "Engineering cryogenic setups for 100-qubit scale superconducting circuit systems.," *European Physical Journal Quantum Technology*, vol. 6, no. 1, pp. 1–29, 2019, ISSN: 26624400.

[10] R. Rehammar and S. Gasparinetti, "Low-pass filter with ultrawide stopband for quantum computing applications," *IEEE Transactions on Microwave Theory and Techniques*, pp. 1–6, 2023. DOI: 10.1109/TMTT.2023.3238543.

[11] G. J. Norris, "Improving infrared-blocking microwave filters," M.S. thesis, ETH Zurich, Oct. 2017.

[12] S. Danilin, J. Barbosa, M. Farage, *et al.*, "Engineering the microwave to infrared noise photon flux for superconducting quantum systems.," *European Physical Journal Quantum Technology*, vol. 9, no. 1, 2022, ISSN: 26624400.

[13] D. M. Pozar, *Microwave engineering*. Wiley, 2012, ISBN: 0470631554.

[14] E. Hammerstad and O. Jensen, "Accurate models for microstrip computer-aided design," in *1980 IEEE MTT-S International Microwave symposium Digest*, 1980, pp. 407–409. DOI: 10.1109/MWSYM.1980.1124303.

[15] P. G. Huray, "Surface roughness," in *The Foundations of Signal Integrity*. 2010, pp. 216–276. DOI: 10.1002/9780470543481.ch6.

[16] C. Robert E., *Foundations for Microwave Engineering*. (IEEE Press Series on Electromagnetic Wave Theory. 11). John Wiley & Sons, 2001, ISBN: 978-0-470-54466-2.

[17] R. E. Collin, "Waveguides and cavities," in *Field Theory of Guided Waves*. 1991, pp. 329–410. DOI: 10.1109/9780470544648.ch5.

[18] O. Shapira, A. F. Abouraddy, J. D. Joannopoulos, and Y. Fink, "Complete modal decomposition for optical waveguides," *Phys. Rev. Lett.*, vol. 94, p. 143 902, 14 Apr. 2005. DOI: 10.1103/PhysRevLett.94.143902.

[19] A. Liu, T. Lin, H. Han, *et al.*, "Analyzing modal power in multi-mode waveguide via machine learning," *Opt. Express*, vol. 26, no. 17, pp. 22 100–22 109, Aug. 2018. DOI: 10.1364/OE.26.022100.

[20] M. Egor S., D. Vladislav V., and T. Sergei K., "Fast mode decomposition in few-mode fibers.," *Nature Communications*, vol. 11, no. 1, pp. 1–9, 2020, ISSN: 2041-1723.

[21] P. S. Anisimov, V. V. Zemlyakov, and J. Gao, "2d least-squares mode decomposition for mode division multiplexing," *Opt. Express*, vol. 30, no. 6, pp. 8804–8813, Mar. 2022. DOI: 10.1364/OE.449393.

[22] R. Brüning, P. Gelszinnis, C. Schulze, D. Flamm, and M. Duparré, "Comparative analysis of numerical methods for the mode analysis of laser beams," *Appl. Opt.*, vol. 52, no. 32, pp. 7769–7777, Nov. 2013. DOI: 10.1364/AO.52.007769.

[23] "Code for the eigenmode field decomposition with field data available at." (May 2023), [Online]. Available: https://github.com/anlinus/EFD.

[24] "RO4350B™ Laminates." (May 2023), [Online]. Available: https://www.rogerscorp.com/advanced-electronics-solutions/ro4000-series-laminates/ro4350b-laminates.

[25] *COMSOL Multiphysics ® v. 6.1* COMSOL AB, Stockholm, Sweden. [Online]. Available: www.comsol.com.

[26] "Shapal Hi M Soft™." (May 2023), [Online]. Available: https://precision-ceramics.com/materials/shapal/.

[27] "Laird™ MF-190." (May 2023), [Online]. Available: https://www.laird.com/products/microwave-absorbers/injection-molded-machined-cast-liquids-and-microwave-absorbing-thermoplastic/eccosorb-mf.

[28] *KiCad EDA v. 7.0*, KiCad. [Online]. Available: www.kicad.org.

[29] B. Rautio and J. Coonrod, "An efficient em simulation model for enig plated metal finishes including conductor side-wall plating verified with physical measurement from 1 to 50 ghz," in *2018 IEEE MTT-S International Microwave Workshop Series on 5G Hardware and System Technologies (IMWS-5G)*, 2018, pp. 1–3. DOI: 10.1109/IMWS-5G.2018.8484386.

[30] W. Frei. “Comsol blog, modeling electromagnetic waves and periodic structures.” (May 2015), [Online]. Available: https://www.comsol.com/blogs/modeling-metallic-objects-in-wave-electromagnetics-problems/.

DEPARTMENT OF SOME SUBJECT OR TECHNOLOGY
CHALMERS UNIVERSITY OF TECHNOLOGY
Gothenburg, Sweden
www.chalmers.se

CHALMERS
UNIVERSITY OF TECHNOLOGY